View metadata, citation and similar papers at core.ac.uk
brought to you by CORE
provided by University of New Mexico

arXiv:1204.0777v1 [nucl-ex] 3 Apr 2012

Transverse-Momentum Dependence of the J/ψ Nuclear Modification in d+Au Collisions at $\sqrt{s_{NN}} = 200$ GeV

A. Adare,[11] S. Afanasiev,[26] C. Aidala,[38] N.N. Ajitanand,[54] Y. Akiba,[49,50] H. Al-Bataineh,[44] J. Alexander,[54] A. Angerami,[12] K. Aoki,[31,49] N. Apadula,[55] Y. Aramaki,[10,49] E.T. Atomssa,[32] R. Averbeck,[55] T.C. Awes,[45] B. Azmoun,[5] V. Babintsev,[21] M. Bai,[4] G. Baksay,[17] L. Baksay,[17] K.N. Barish,[6] B. Bassalleck,[43] A.T. Basye,[1] S. Bathe,[6,50] V. Baublis,[48] C. Baumann,[39] A. Bazilevsky,[5] S. Belikov,[5,*] R. Belmont,[59] R. Bennett,[55] A. Berdnikov,[52] Y. Berdnikov,[52] J.H. Bhom,[63] D.S. Blau,[30] J.S. Bok,[63] K. Boyle,[55] M.L. Brooks,[34] H. Buesching,[5] V. Bumazhnov,[21] G. Bunce,[5,50] S. Butsyk,[34] S. Campbell,[55] A. Caringi,[40] C.-H. Chen,[55] C.Y. Chi,[12] M. Chiu,[5] I.J. Choi,[63] J.B. Choi,[8] R.K. Choudhury,[3] P. Christiansen,[36] T. Chujo,[58] P. Chung,[54] O. Chvala,[6] V. Cianciolo,[45] Z. Citron,[55] B.A. Cole,[12] Z. Conesa del Valle,[32] M. Connors,[55] M. Csanád,[15] T. Csörgő,[62] T. Dahms,[55] S. Dairaku,[31,49] I. Danchev,[59] K. Das,[18] A. Datta,[38] G. David,[5] M.K. Dayananda,[19] A. Denisov,[21] A. Deshpande,[50,55] E.J. Desmond,[5] K.V. Dharmawardane,[44] O. Dietzsch,[53] A. Dion,[25] M. Donadelli,[53] O. Drapier,[32] A. Drees,[55] K.A. Drees,[4] J.M. Durham,[55] A. Durum,[21] D. Dutta,[3] L. D'Orazio,[37] S. Edwards,[18] Y.V. Efremenko,[45] F. Ellinghaus,[11] T. Engelmore,[12] A. Enokizono,[45] H. En'yo,[49,50] S. Esumi,[58] B. Fadem,[40] D.E. Fields,[43] M. Finger,[7] M. Finger, Jr.,[7] F. Fleuret,[32] S.L. Fokin,[30] Z. Fraenkel,[61,*] J.E. Frantz,[55] A. Franz,[5] A.D. Frawley,[18] K. Fujiwara,[49] Y. Fukao,[49] T. Fusayasu,[42] I. Garishvili,[56] A. Glenn,[33] H. Gong,[55] M. Gonin,[32] Y. Goto,[49,50] R. Granier de Cassagnac,[32] N. Grau,[12] S.V. Greene,[59] G. Grim,[34] M. Grosse Perdekamp,[22] T. Gunji,[10] H.-Å. Gustafsson,[36,*] J.S. Haggerty,[5] K.I. Hahn,[16] H. Hamagaki,[10] J. Hamblen,[56] R. Han,[47] J. Hanks,[12] E. Haslum,[36] R. Hayano,[10] X. He,[19] M. Heffner,[33] T.K. Hemmick,[55] T. Hester,[6] J.C. Hill,[25] M. Hohlmann,[17] W. Holzmann,[12] K. Homma,[20] B. Hong,[29] T. Horaguchi,[20] D. Hornback,[56] S. Huang,[59] T. Ichihara,[49,50] R. Ichimiya,[49] Y. Ikeda,[58] K. Imai,[31,49] M. Inaba,[58] D. Isenhower,[1] M. Ishihara,[49] M. Issah,[59] A. Isupov,[26] D. Ivanischev,[48] Y. Iwanaga,[20] B.V. Jacak,[55,†] J. Jia,[5,54] X. Jiang,[34] J. Jin,[12] B.M. Johnson,[5] T. Jones,[1] K.S. Joo,[41] D. Jouan,[46] D.S. Jumper,[1] F. Kajihara,[10] J. Kamin,[55] J.H. Kang,[63] J. Kapustinsky,[34] K. Karatsu,[31,49] M. Kasai,[49,51] D. Kawall,[38,50] M. Kawashima,[49,51] A.V. Kazantsev,[30] T. Kempel,[25] A. Khanzadeev,[48] K.M. Kijima,[20] J. Kikuchi,[60] A. Kim,[16] B.I. Kim,[29] D.J. Kim,[27] E.J. Kim,[8] Y.-J. Kim,[22] E. Kinney,[11] Á. Kiss,[15] E. Kistenev,[5] D. Kleinjan,[6] L. Kochenda,[48] B. Komkov,[48] M. Konno,[58] J. Koster,[22] A. Král,[13] A. Kravitz,[12] G.J. Kunde,[34] K. Kurita,[49,51] M. Kurosawa,[49] Y. Kwon,[63] G.S. Kyle,[44] R. Lacey,[54] Y.S. Lai,[12] J.G. Lajoie,[25] A. Lebedev,[25] D.M. Lee,[34] J. Lee,[16] K.B. Lee,[29] K.S. Lee,[29] M.J. Leitch,[34] M.A.L. Leite,[53] X. Li,[9] P. Lichtenwalner,[40] P. Liebing,[50] L.A. Linden Levy,[11] T. Liška,[13] A. Litvinenko,[26] H. Liu,[34] M.X. Liu,[34] B. Love,[59] D. Lynch,[5] C.F. Maguire,[59] Y.I. Makdisi,[4] A. Malakhov,[26] M.D. Malik,[43] V.I. Manko,[30] E. Mannel,[12] Y. Mao,[47,49] H. Masui,[58] F. Matathias,[12] M. McCumber,[55] P.L. McGaughey,[34] D. McGlinchey,[18] N. Means,[55] B. Meredith,[22] Y. Miake,[58] T. Mibe,[28] A.C. Mignerey,[37] K. Miki,[49,58] A. Milov,[5] J.T. Mitchell,[5] A.K. Mohanty,[3] H.J. Moon,[41] Y. Morino,[10] A. Morreale,[6] D.P. Morrison,[5] T.V. Moukhanova,[30] T. Murakami,[31] J. Murata,[49,51] S. Nagamiya,[28] J.L. Nagle,[11] M. Naglis,[61] M.I. Nagy,[62] I. Nakagawa,[49,50] Y. Nakamiya,[20] K.R. Nakamura,[31,49] T. Nakamura,[49] K. Nakano,[49] S. Nam,[16] J. Newby,[33] M. Nguyen,[55] M. Nihashi,[20] R. Nouicer,[5] A.S. Nyanin,[30] C. Oakley,[19] E. O'Brien,[5] S.X. Oda,[10] C.A. Ogilvie,[25] M. Oka,[58] K. Okada,[50] Y. Onuki,[49] A. Oskarsson,[36] M. Ouchida,[20,49] K. Ozawa,[10] R. Pak,[5] V. Pantuev,[23,55] V. Papavassiliou,[44] I.H. Park,[16] S.K. Park,[29] W.J. Park,[29] S.F. Pate,[44] H. Pei,[25] J.-C. Peng,[22] H. Pereira,[14] V. Peresedov,[26] D.Yu. Peressounko,[30] R. Petti,[55] C. Pinkenburg,[5] R.P. Pisani,[5] M. Proissl,[55] M.L. Purschke,[5] H. Qu,[19] J. Rak,[27] I. Ravinovich,[61] K.F. Read,[45,56] S. Rembeczki,[17] K. Reygers,[39] V. Riabov,[48] Y. Riabov,[48] E. Richardson,[37] D. Roach,[59] G. Roche,[35] S.D. Rolnick,[6] M. Rosati,[25] C.A. Rosen,[11] S.S.E. Rosendahl,[36] P. Rukoyatkin,[26] P. Ružička,[24] B. Sahlmueller,[39] N. Saito,[28] T. Sakaguchi,[5] K. Sakashita,[49,57] V. Samsonov,[48] S. Sano,[10,60] T. Sato,[58] S. Sawada,[28] K. Sedgwick,[6] J. Seele,[11] R. Seidl,[22,50] R. Seto,[6] D. Sharma,[61] I. Shein,[21] T.-A. Shibata,[49,57] K. Shigaki,[20] M. Shimomura,[58] K. Shoji,[31,49] P. Shukla,[3] A. Sickles,[5] C.L. Silva,[25] D. Silvermyr,[45] C. Silvestre,[14] K.S. Sim,[29] B.K. Singh,[2] C.P. Singh,[2] V. Singh,[2] M. Slunečka,[7] R.A. Soltz,[33] W.E. Sondheim,[34] S.P. Sorensen,[56] I.V. Sourikova,[5] P.W. Stankus,[45] E. Stenlund,[36] S.P. Stoll,[5] T. Sugitate,[20] A. Sukhanov,[5] J. Sziklai,[62] E.M. Takagui,[53] A. Taketani,[49,50] R. Tanabe,[58] Y. Tanaka,[42] S. Taneja,[55] K. Tanida,[31,49,50] M.J. Tannenbaum,[5] S. Tarafdar,[2] A. Taranenko,[54] H. Themann,[55] D. Thomas,[1] T.L. Thomas,[43] M. Togawa,[50] A. Toia,[55] L. Tomášek,[24] H. Torii,[20] R.S. Towell,[1] I. Tserruya,[61] Y. Tsuchimoto,[20] C. Vale,[5] H. Valle,[59] H.W. van Hecke,[34] E. Vazquez-Zambrano,[12] A. Veicht,[22] J. Velkovska,[59] R. Vértesi,[62] M. Virius,[13] V. Vrba,[24] E. Vznuzdaev,[48] X.R. Wang,[44] D. Watanabe,[20] K. Watanabe,[58] Y. Watanabe,[49,50] F. Wei,[25] R. Wei,[54] J. Wessels,[39] S.N. White,[5] D. Winter,[12] C.L. Woody,[5] R.M. Wright,[1] M. Wysocki,[11] Y.L. Yamaguchi,[10] K. Yamaura,[20] R. Yang,[22] A. Yanovich,[21] J. Ying,[19]

S. Yokkaichi,[49,50] Z. You,[47] G.R. Young,[45] I. Younus,[43] I.E. Yushmanov,[30] W.A. Zajc,[12] S. Zhou,[9] and L. Zolin[26]
(PHENIX Collaboration)

[1]*Abilene Christian University, Abilene, Texas 79699, USA*
[2]*Department of Physics, Banaras Hindu University, Varanasi 221005, India*
[3]*Bhabha Atomic Research Centre, Bombay 400 085, India*
[4]*Collider-Accelerator Department, Brookhaven National Laboratory, Upton, New York 11973-5000, USA*
[5]*Physics Department, Brookhaven National Laboratory, Upton, New York 11973-5000, USA*
[6]*University of California - Riverside, Riverside, California 92521, USA*
[7]*Charles University, Ovocný trh 5, Praha 1, 116 36, Prague, Czech Republic*
[8]*Chonbuk National University, Jeonju, 561-756, Korea*
[9]*Science and Technology on Nuclear Data Laboratory, China Institute of Atomic Energy, Beijing 102413, P. R. China*
[10]*Center for Nuclear Study, Graduate School of Science, University of Tokyo, 7-3-1 Hongo, Bunkyo, Tokyo 113-0033, Japan*
[11]*University of Colorado, Boulder, Colorado 80309, USA*
[12]*Columbia University, New York, New York 10027 and Nevis Laboratories, Irvington, New York 10533, USA*
[13]*Czech Technical University, Zikova 4, 166 36 Prague 6, Czech Republic*
[14]*Dapnia, CEA Saclay, F-91191, Gif-sur-Yvette, France*
[15]*ELTE, Eötvös Loránd University, H - 1117 Budapest, Pázmány P. s. 1/A, Hungary*
[16]*Ewha Womans University, Seoul 120-750, Korea*
[17]*Florida Institute of Technology, Melbourne, Florida 32901, USA*
[18]*Florida State University, Tallahassee, Florida 32306, USA*
[19]*Georgia State University, Atlanta, Georgia 30303, USA*
[20]*Hiroshima University, Kagamiyama, Higashi-Hiroshima 739-8526, Japan*
[21]*IHEP Protvino, State Research Center of Russian Federation, Institute for High Energy Physics, Protvino, 142281, Russia*
[22]*University of Illinois at Urbana-Champaign, Urbana, Illinois 61801, USA*
[23]*Institute for Nuclear Research of the Russian Academy of Sciences, prospekt 60-letiya Oktyabrya 7a, Moscow 117312, Russia*
[24]*Institute of Physics, Academy of Sciences of the Czech Republic, Na Slovance 2, 182 21 Prague 8, Czech Republic*
[25]*Iowa State University, Ames, Iowa 50011, USA*
[26]*Joint Institute for Nuclear Research, 141980 Dubna, Moscow Region, Russia*
[27]*Helsinki Institute of Physics and University of Jyväskylä, P.O.Box 35, FI-40014 Jyväskylä, Finland*
[28]*KEK, High Energy Accelerator Research Organization, Tsukuba, Ibaraki 305-0801, Japan*
[29]*Korea University, Seoul, 136-701, Korea*
[30]*Russian Research Center "Kurchatov Institute", Moscow, 123098 Russia*
[31]*Kyoto University, Kyoto 606-8502, Japan*
[32]*Laboratoire Leprince-Ringuet, Ecole Polytechnique, CNRS-IN2P3, Route de Saclay, F-91128, Palaiseau, France*
[33]*Lawrence Livermore National Laboratory, Livermore, California 94550, USA*
[34]*Los Alamos National Laboratory, Los Alamos, New Mexico 87545, USA*
[35]*LPC, Université Blaise Pascal, CNRS-IN2P3, Clermont-Fd, 63177 Aubiere Cedex, France*
[36]*Department of Physics, Lund University, Box 118, SE-221 00 Lund, Sweden*
[37]*University of Maryland, College Park, Maryland 20742, USA*
[38]*Department of Physics, University of Massachusetts, Amherst, Massachusetts 01003-9337, USA*
[39]*Institut fur Kernphysik, University of Muenster, D-48149 Muenster, Germany*
[40]*Muhlenberg College, Allentown, Pennsylvania 18104-5586, USA*
[41]*Myongji University, Yongin, Kyonggido 449-728, Korea*
[42]*Nagasaki Institute of Applied Science, Nagasaki-shi, Nagasaki 851-0193, Japan*
[43]*University of New Mexico, Albuquerque, New Mexico 87131, USA*
[44]*New Mexico State University, Las Cruces, New Mexico 88003, USA*
[45]*Oak Ridge National Laboratory, Oak Ridge, Tennessee 37831, USA*
[46]*IPN-Orsay, Universite Paris Sud, CNRS-IN2P3, BP1, F-91406, Orsay, France*
[47]*Peking University, Beijing 100871, P. R. China*
[48]*PNPI, Petersburg Nuclear Physics Institute, Gatchina, Leningrad region, 188300, Russia*
[49]*RIKEN Nishina Center for Accelerator-Based Science, Wako, Saitama 351-0198, Japan*
[50]*RIKEN BNL Research Center, Brookhaven National Laboratory, Upton, New York 11973-5000, USA*
[51]*Physics Department, Rikkyo University, 3-34-1 Nishi-Ikebukuro, Toshima, Tokyo 171-8501, Japan*
[52]*Saint Petersburg State Polytechnic University, St. Petersburg, 195251 Russia*
[53]*Universidade de São Paulo, Instituto de Física, Caixa Postal 66318, São Paulo CEP05315-970, Brazil*
[54]*Chemistry Department, Stony Brook University, SUNY, Stony Brook, New York 11794-3400, USA*
[55]*Department of Physics and Astronomy, Stony Brook University, SUNY, Stony Brook, New York 11794-3400, USA*
[56]*University of Tennessee, Knoxville, Tennessee 37996, USA*
[57]*Department of Physics, Tokyo Institute of Technology, Oh-okayama, Meguro, Tokyo 152-8551, Japan*
[58]*Institute of Physics, University of Tsukuba, Tsukuba, Ibaraki 305, Japan*
[59]*Vanderbilt University, Nashville, Tennessee 37235, USA*
[60]*Waseda University, Advanced Research Institute for Science and Engineering, 17 Kikui-cho, Shinjuku-ku, Tokyo 162-0044, Japan*

[61] Weizmann Institute, Rehovot 76100, Israel
[62] Institute for Particle and Nuclear Physics, Wigner Research Centre for Physics, Hungarian Academy of Sciences (Wigner RCP, RMKI) H-1525 Budapest 114, POBox 49, Budapest, Hungary
[63] Yonsei University, IPAP, Seoul 120-749, Korea

(Dated: April 4, 2012)

We present measured J/ψ production rates in d+Au collisions at $\sqrt{s_{NN}} = 200$ GeV over a broad range of transverse momentum (p_T = 0–14 GeV/c) and rapidity ($-2.2 < y < 2.2$). We construct the nuclear-modification factor $R_{d\mathrm{Au}}$ for these kinematics and as a function of collision centrality (related to impact parameter for the $R_{d\mathrm{Au}}$ collision). We find that the modification is largest for collisions with small impact parameters, and observe a suppression ($R_{d\mathrm{Au}} < 1$) for $p_T < 4$ GeV/c at positive rapidities. At negative rapidity we observe a suppression for $p_T < 2$ GeV/c then an enhancement ($R_{d\mathrm{Au}} > 1$) for $p_T > 2$ GeV/c. The observed enhancement at negative rapidity has implications for the observed modification in heavy-ion collisions at high p_T.

PACS numbers: 25.75.Dw

I. INTRODUCTION

Modifications of quarkonia yields when production takes place in a nuclear target, often termed cold-nuclear-matter (CNM) effects, give insight into the production and evolution of $q\bar{q}$ pairs. A number of effects are predicted to occur in the presence of nuclear matter (for a recent review, see [1]). These include nuclear breakup, modification of the parton-distribution functions, initial-state parton-energy loss and, more recently, coherent gluon saturation. Measuring the production rate of quarkonia in a nuclear environment over a broad range of collision energies, and as a function of all kinematic variables, is the best way to disentangle these different mechanisms.

The measurement of J/ψ production rates over a broad range of rapidity (y) and transverse momentum (p_T) samples a wide range of parton momentum fraction (x) and energy transfer (Q^2), providing a simultaneous constraint on the modification of parton-distribution functions inside nuclei (nPDF's). The production of J/ψ mesons, which at RHIC occurs mainly through gluon fusion, can provide critical input on the modification of the gluon distribution, which is probed only indirectly by the deep-inelastic scattering (DIS) data that forms the bulk of the current constraints on the nPDF parametrizations.

Measuring the p_T distribution of J/ψ production allows access to p_T-broadening effects, which are not constrained by measurements of the rapidity dependence alone. The p_T-broadening effects on quarkonia production at high energies are not well constrained by current data. New data for J/ψ production over a broad range in p_T is necessary to provide guidance for theoretical calculations.

The CNM effects on J/ψ production have been studied in fixed-target $p+A$ experiments at SPS, FNAL, and HERA [2–8] spanning the center of mass energy range $\sqrt{s} \approx 17 - 42$ GeV. The fixed-target results at midrapidity show greater suppression of J/ψ production at lower collision energy [6]. This has been interpreted [9] as an increase of the nuclear breakup of the J/ψ through collisions with nuclei. At lower collision energy the crossing time of the nuclei is long enough for the J/ψ to fully form. The fully formed J/ψ has an increased probability of interacting with other nucleons in the collision, which can cause the breakup of the J/ψ into heavy-meson pairs. At higher collision energies it is likely that the time required for the J/ψ to fully evolve is as long, or longer than the crossing time of the collision. This may result in a decrease in the probability of collisions with other nucleons, leading to less suppression of the J/ψ production.

The E866 [7] and HERA-B [8] experiments have measured J/ψ production as a function of p_T in fixed target $p+A$ experiments. Results are presented in terms of the nuclear-suppression factor, α, which is obtained assuming that the cross section for $p+A$ collisions scales as $\sigma_{pA} = \sigma_{pN} \times A^{\alpha}$, where σ_{pN} is the proton-nucleon cross section and A is the mass number. They find a p_T dependence of α, which is similar across a range of Feynman-x (x_F) and p_T. At $p_T < 2$ GeV/c they find a suppression in the J/ψ production that transitions to an excess in the J/ψ production at higher p_T, which is characteristic of multiple scattering of the incident parton [7]. It is crucial to test these conclusions at the higher energies provided by d+Au collisions at RHIC in order to better understand the J/ψ production mechanisms.

Measuring, and understanding, the CNM effects on quarkonia production is critical to interpreting the results for J/ψ production in nucleus-nucleus ($A+A$) collisions. In 1986 Matsui and Satz predicted that the suppression of J/ψ production in heavy-ion collisions would be a clear signature of the formation of a quark-gluon plasma [10]. The Debye color screening of the dense medium produced is expected to cause the dissociation of bound states, thereby causing a decrease in the observed production. Since then suppression of quarkonia production has been observed for a number of states, including the J/ψ and Υ, over a wide range in collision energy [11–14]. However, the interpretation of these results is still unclear. Before

*Deceased
†PHENIX Spokesperson: jacak@skipper.physics.sunysb.edu

the modification due to the produced medium can be determined, the CNM effects must first be corrected. This has been done at lower energies [11], but accurate data on CNM effects are still absent at the higher energies of RHIC and the LHC.

Here we report new high-precision measurements of the J/ψ production as a function of p_T and collision centrality in d+Au collisions at $\sqrt{s_{NN}} = 200$ GeV. We also present measurements of the J/ψ $R_{\rm dAu}$ as a function of p_T, rapidity, and collision centrality using data for J/ψ production in p+p collisions published in [15]. PHENIX has previously measured the J/ψ yield in d+Au collisions [16, 17] with data recorded in 2003. The data presented here, recorded in 2008, feature an increase in statistics of 30–50 times over those used in the previously published results, as well as a significant reduction of the systematic uncertainties. The rapidity dependence of J/ψ production in d+Au collisions from this data set has been previously published in [18]. This paper presents results for the p_T dependence of the J/ψ yield from the same data set.

II. EXPERIMENTAL APPARATUS & DATA SETS

The PHENIX detector [19] comprises three separate spectrometers in three pseudorapidity (η) ranges. Two central arms at midrapidity cover $|\eta| < 0.35$ and have an azimuthal coverage (ϕ) of $\pi/2$ rad each, while muon arms at backward/forward rapidity cover $-2.2 < \eta < -1.2$ (Au going direction) and $1.2 < \eta < 2.4$ (d going direction), with full azimuthal coverage.

In the central arms the J/ψ yield is measured via dielectron decays. Charged particle tracks are reconstructed using the drift chamber and pad chambers. Electron candidates are selected by matching charged tracks to hits in the ring imaging Čerenkov (RICH) counters and clusters in the Electromagnetic Calorimeters (EMCal). In d+Au collisions, a charged track is identified as an electron by requiring at least two matching RICH phototube hits within a radius of $3.4 < R[cm] < 8.4$ with respect to the center defined by the track projection at the RICH. It is also required that the position of the EMCal cluster associated to the track projection match within $\pm 4\sigma$, and that the ratio of the energy deposited in the EMCal cluster to the momentum of the tracks matches unity within $\pm 2.5\sigma$, where σ characterizes the momentum dependent width of the matching distributions. A further cut of 200 MeV/c on the momentum of the electron is added to reduce the combinatorial background, since the yield of electrons from J/ψ decays observed in data and simulations is negligible below 200 MeV/c .

At forward and backward rapidity, the J/ψ yield is measured via dimuon decays. Muons are identified by matching tracks measured in cathode-strip chambers, referred to as the muon tracker (MuTr), to hits in alternating planes of Iarocci tubes and steel absorbers, referred to as the muon identifier (MuID). Each muon arm is located behind a thick copper and iron absorber that is meant to stop most hadrons produced during the collisions, so that the detected muons must penetrate 8 to 11 interaction lengths of material in total.

Beam interactions are selected with a minimum-bias (MB) trigger requiring at least one hit in each of two beam-beam counters (BBCs) located at positive and negative pseudorapidity $3 < |\eta| < 3.9$. The MB selection covers $88 \pm 4\%$ of the total d+Au inelastic cross section of 2260 mb [20].

The d+Au data sample used in this analysis requires the MB trigger to be in coincidence with an additional Level-1 trigger. For electrons, this is a single electron EMCal RICH trigger (ERT), which requires a minimum energy deposited in any 2×2 group of EMCal towers, plus an associated hit in the RICH. Two thresholds on the minimum EMCal energy, 600 MeV and 800 MeV, were used, each for roughly half of the data sample. For muons, the level 1 trigger requires two tracks identified as muon candidates. The trigger logic for a muon candidate requires a "road" of fired Iarocci tubes in at least 4 planes, including the most downstream plane relative to the collision point. Additionally, collisions are required to be within ±30cm of the center of the interaction region. Collisions in that range see the full geometric acceptance of the central arms, and this cut also provides a reduction of the systematic uncertainties on the centrality selection needed for the data from the muon arms. The data sets sampled via the Level-1 triggers represent analyzed integrated luminosities of 62.7 nb^{-1} (electrons) and 54.0 nb^{-1} (muons) and nucleon-nucleon integrated luminosities of 24.7 pb^{-1} and 21.3 pb^{-1} respectively.

TABLE I: Characterization of the collision centrality for d+Au collisions along with the correction factor c (see text for details).

Centrality	$\langle N_{\rm coll}\rangle$	c	$c/\langle N_{\rm coll}\rangle$
0–20 %	15.1 ± 1.0	0.94 ± 0.01	0.062 ± 0.003
20–40 %	10.2 ± 0.7	1.000 ± 0.006	0.098 ± 0.004
40–60 %	6.6 ± 0.4	1.03 ± 0.02	0.157 ± 0.008
60–88 %	3.2 ± 0.2	1.03 ± 0.06	0.33 ± 0.02
0–100 %	7.6 ± 0.4	0.889 ± 0.001	0.117 ± 0.004

The centrality, which is related to the impact parameter, b, of the d+Au collision is determined using the total charge deposited in the BBC located at negative rapidity (Au-going direction). The centrality is defined as a percentage of the total charge distribution referenced to the greatest charge, *i.e.* 0–20% refers to the 20% of the total charge distribution with the greatest charge. On average the 0–20% centrality corresponds to collisions with the smallest b.

For each centrality bin the mean number of nucleon-nucleon collisions ($\langle N_{\rm coll}\rangle$) is determined using a Glauber calculation [21] combined with a simulation of the BBC

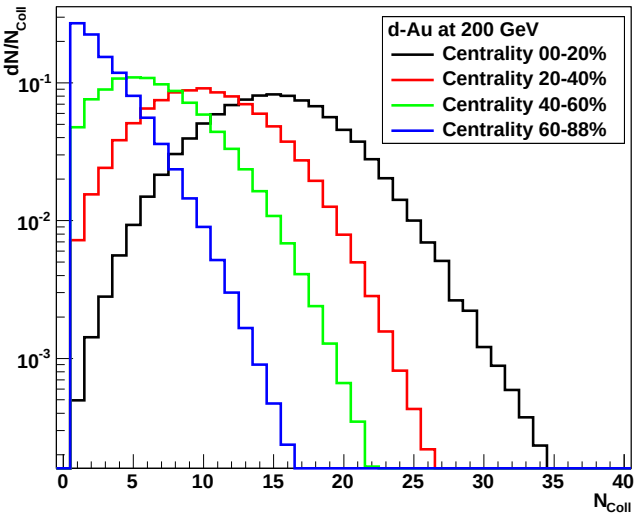

FIG. 1: (Color online) Nucleon-nucleon collision ($N_{\rm coll}$) distributions for each centrality bin obtained using a Glauber model for d+Au collisions described in the text.

response (as described in [18]). The resulting $\langle N_{\rm coll}\rangle$ values for the centrality categories used in this analysis are shown in Table I. The $N_{\rm coll}$ distributions within each centrality bin are shown in Fig. 1. There is a significant overlap between the $N_{\rm coll}$ distributions for different centralities.

Also shown in Table I is the correction factor c, which accounts for the correlation between the detection of a J/ψ in the final state and an increase in the total charge collected in the BBC [16]. This correlation affects both the MB-trigger efficiency and the determination of the centrality of a given collision. The correction factors for each centrality bin are obtained within the same Glauber framework as the $\langle N_{\rm coll}\rangle$ values by assuming that one of the N binary collisions produces a charge in the BBC that is characteristic of a hard-scattering process (the remaining N-1 binary collisions maintain a BBC charge distribution characteristic of soft scattering processes). The increase in the BBC charge from a hard process is tuned using real data.

Since both c and $\langle N_{\rm coll}\rangle$ are calculated in the same Glauber framework there are correlations between their uncertainties. These correlations are removed in the ratio of $c/\langle N_{\rm coll}\rangle$, which occurs in the calculation of $R_{d\rm Au}$. The resulting values and uncertainties are given in the third column of Table I. The correction factor for 0–100% centrality contains an additional factor to extrapolate the measured yield, which covers only 88% of all d+Au collisions, to 100% of the d+Au inelastic cross section, essentially correcting for the efficiency of the BBC trigger. This correction is again determined within the Glauber framework using the parametrization of the BBC trigger efficiency.

III. J/ψ ANALYSIS AND RESULTS IN THE MIDRAPIDITY REGION

The procedure for analyzing the $J/\psi \to e^+e^-$ signal and the results in the central arms are discussed in this section. The extraction of the correlated e^+e^- yield is discussed in Sec. III A. The estimation of the correlated background and losses due to the radiative tail in the J/ψ mass distribution is discussed in Sec. III B. The estimation of the detector efficiencies is described in Sec. III C. The calculation of the J/ψ invariant yield is detailed in Sec. III D. The p+p baseline used in calculating $R_{d\rm Au}$ is described in Sec. III E.

A. Correlated e^+e^- Signal extraction

The $J/\psi \to e^+e^-$ yield is measured using the invariant mass spectrum for all dielectron pairs where at least one of the electrons fired the ERT trigger. This selection is necessary to match the conditions under which the J/ψ trigger efficiency is calculated (see Sec. III C). An example of the dielectron mass spectrum is shown in Fig. 2 for 0–20% central collisions. In a given bin of p_T, rapidity, and collision centrality, the correlated e^+e^- yield ($N_{e^+e^-}$) is determined by counting over a fixed mass window of $2.8 < M_{ee}\,[{\rm GeV}/c^2\,] < 3.3$ the number of unlike-sign dielectrons, after the subtraction of the like-sign dielectrons, which arise by random association and so are representative of the combinatorial background within the unlike sign dielectron distribution. This method assumes that the acceptance is the same for e^- and e^+, which, while untrue at lower masses, is a good assumption in the J/ψ mass range. At higher p_T, where statistical precision is limited, the yield, along with the statistical uncertainties, are derived from Poisson statistics. Assuming both the unlike-sign (foreground) and like-sign (background) are independent, and assuming no negative signal, the combined distribution

$$P(s) = \sum_{k=0}^{fg} \frac{(bg+fg-k)!}{bg!(fg-k)!}\frac{1}{2}\left(\frac{1}{2}\right)^{bg+fg-k}\frac{s^k e^{-s}}{k!}, \quad (1)$$

represents the probability of a signal (s) given a number of unlike-sign dielectrons (fg) and a number of like-sign dielectrons (bg) (see [15] for derivation). The mean and standard deviation of Eq. 1 are then used as the yield and uncertainties. A correlated e^+e^- yield in the mass window $2.8 < M_{ee}\,[{\rm GeV}/c^2\,] < 3.3$ of approximately 8600 is obtained across all p_T and collision centralities.

B. Estimation of the Correlated Background and Losses Due to the Radiative Tail in the J/ψ Mass Distribution

When using the like-sign subtraction method there remains a correlated background under the observed J/ψ

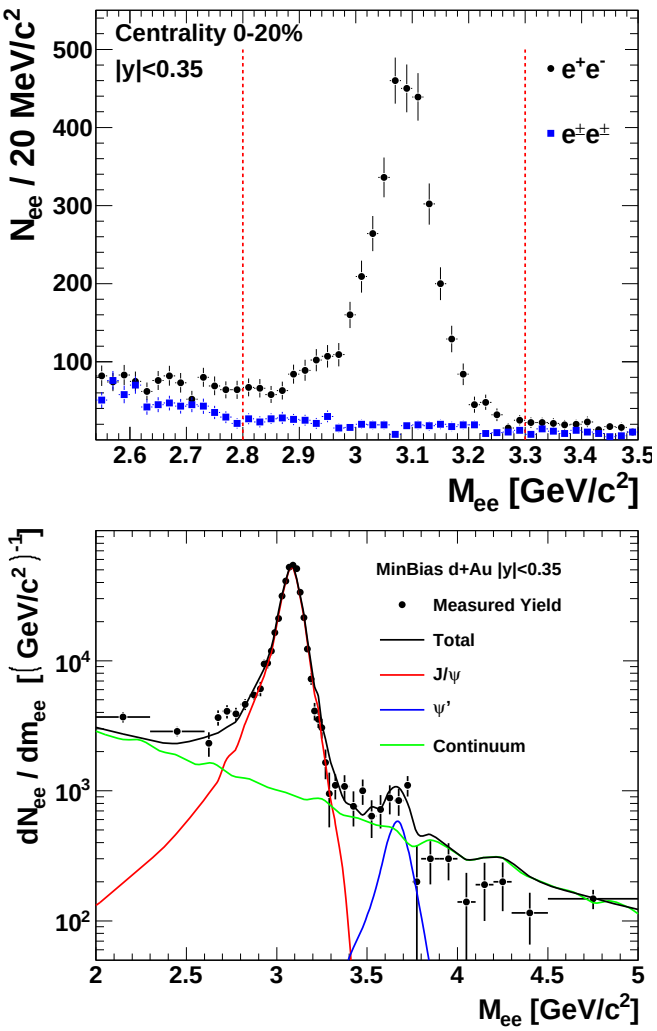

FIG. 2: (Color online) (top) Invariant mass distribution of unlike-sign (filled circles) and like-sign (filled boxes) dielectron pairs in central d+Au collisions, integrated over p_T and rapidity. Dashed vertical lines represent the mass range used to determine the correlated e^+e^- yield. (bottom) Correlated dielectron invariant mass distribution for MB d+Au collisions. The line shapes are those used to extract the continuum and radiative tail contributions to the correlated e^+e^- yield in the mass range $2.8 < M_{ee}\,[\mathrm{GeV}/c^2\,] < 3.3$.

peak. This background comes mainly from open-heavy-flavor decays and Drell-Yan pairs, and must be separated from the J/ψ signal of interest. Counting the dielectron signal only over a fixed mass window also causes an underestimate of the J/ψ yield due to the fraction of the J/ψ line shape that falls outside the mass window of choice. These two effects are quantified by using simulated particle line shapes fitted to the real data distribution.

The J/ψ and ψ' mesons with uniform distributions in p_T ($0 < p_T\,[\mathrm{GeV}/c\,] < 12$) and rapidity ($|y| < 0.35$) are decayed to e^+e^- and the external radiation effects are evaluated using a GEANT-3 based model of the PHENIX detector (described in Sec. III C). While a uniform distribution in p_T is unrealistic, the J/ψ rapidity distribution is roughly constant within $|y| < 0.35$. When used here, the J/ψ and ψ' line shapes will be compared to p_T integrated data as a function of invariant mass only, with a mass resolution fitted to the data, and therefore the effect of using a uniform p_T distribution is negligible. The line shape for J/ψ radiative decays ($J/\psi \to e^+e^-\gamma$), also called internal radiation, is based on calculations of the mass distribution from QED [22] convoluted with the detector resolution.

Line shapes for the correlated background from heavy-flavor decays along with Drell-Yan pairs are simulated using PYTHIA [23]. The correlated background from heavy-flavor decays comes from semi-leptonic decays of correlated $D\bar{D}$ and $B\bar{B}$ (i.e. $D \to e^+ + X$ and $\bar{D} \to e^- + X$). The decay electrons from PYTHIA are then run through the same GEANT simulation of the PHENIX detector to evaluate the external radiation effects. These line shapes are generated assuming $p + p$ collisions, and no corrections for CNM effects (i.e. application of nPDF modifications) are applied to the distributions. We assume that the CNM effects on these distributions are likely small and roughly constant over the narrow mass window used due to the x values probed. No suppression of heavy-flavor production has been observed in d+Au collisions, and we assume that any suppression, if it exists, does not significantly effect the overall line shapes.

The line shapes are then fitted to the p_T and collision centrality integrated invariant mass spectrum over the mass range $2 < M_{ee}\,[\mathrm{GeV}/c^2\,] < 8$ where the normalizations on the J/ψ, ψ', correlated heavy flavor, and DY are free to vary independently. The best fit is shown in the quarkonium mass region in Fig. 2, where the continuum line shape is the combination of correlated e^+e^- pairs from $D\bar{D}$, $B\bar{B}$, and DY decays, and the J/ψ and ψ' line shapes are the combinations of the line shapes from both internal and external radiation effects. Within the mass window $2.8 < M_{ee}\,[\mathrm{GeV}/c^2\,] < 3.3$ the correlated continuum contribution (ϵ_{cont}) is found to be $6.6 \pm 0.2\%$ and the fraction of the J/ψ line shape contained within the mass window (ϵ_{rad}) to be $94.3 \pm 0.2\%$, where the uncertainties are derived from the uncertainty in the fit. The disagreement between the fit and the data in the $3.7 < M_{ee}\,[\mathrm{GeV}/c^2\,] < 4.5$ mass range is likely due to the inability of the $D\bar{D}$ and $B\bar{B}$ line shapes to match the shape of the data at higher mass. However, large changes in the ratio of their contributions have only a small effect on the extracted values of ϵ_{cont} and ϵ_{rad}, and this is accounted for in the quoted uncertainties.

C. Acceptance and Efficiency Studies

The J/ψ acceptance is investigated using a GEANT-3 [24] based Monte Carlo model of the PHENIX detector. Dead and malfunctioning channels in the detector are removed from both the detector simulation and real data.

The accuracy of the simulations is tested by comparing simulated single electron distributions with those from real data. The agreement across the detector and data taking period is determined to be within 3.2%. A conservative estimate, which assumes that the uncertainty is correlated for both electrons in a pair, of $2 \times 3.2\% = 6.4\%$ is assigned as a systematic uncertainty on the J/ψ acceptance based on the quality of the matching between simulations and data.

To determine the J/ψ acceptance, $J/\psi \to e^+e^-$ decays are simulated with uniform distributions in p_T, rapidity ($|y| < 0.5$) and collision vertex. While distributions uniform in p_T are not realistic, the corrections are made over a small p_T bin where the real distribution can be approximated as linear. This assumption, and the effect of bin sharing, is tested later and taken into account when assigning systematic uncertainties. The fraction of J/ψ decays that are reconstructed corresponds to the combination of the geometric acceptance and the electron ID efficiency ($A \times \epsilon_{\rm eID}$). The resulting $A \times \epsilon_{\rm eID}$ is shown as a function of p_T in Fig. 3. It has an average value of 1.5% in 1 unit of rapidity. The dip in $A \times \epsilon_{eID}$ followed by a continual increase with p_T marks the transition from the e^+e^- pair at low p_T being produced back to back and being detected one in each of the PHENIX central arms, to the pair at high p_T being produced in a collinear manner and being detected both in the same PHENIX central arm. The low point at $p_T \approx 3$ GeV/c corresponds to the e^+e^- being produced at roughly 90° relative to each other in the lab frame, which due to the PHENIX geometry has the lowest probability for detection. The electron ID efficiency, which is mainly due to track reconstruction cuts used to avoid the misidentification of hadrons as electrons, was cross checked using electrons from π^0 Dalitz decays and γ conversions as described in [15], and a systematic uncertainty of 1.1% is assigned based on that comparison. The effect of momentum smearing on the electrons in simulations, which can cause a J/ψ to be reconstructed into a different p_T bin than the one it was generated in, was also investigated. The effect was found to be minimal for all but the highest p_T bins and an uncertainty of 0.2% was assigned based on a Monte-Carlo study effect and a parametrization of the measured momentum resolution for electrons. A combined uncertainty of 6.5% is assigned to the J/ψ $A \times \epsilon_{eID}$ by adding the simulation/data matching, eID, and momentum smearing uncertainties in quadrature.

The ERT trigger efficiency is evaluated using simulations of J/ψ decays and parametrizations of the single electron trigger efficiencies in each trigger tile. A MB data sample of single electrons is used to measure the p_T dependent efficiency of each 2x2 EMCal trigger tile and each RICH trigger tile independently by calculating the fraction of electrons that fired the trigger tile compared to all those passing through it. The resulting distributions are then fitted with an error(uniform) function for each trigger tile in the EMCal(RICH). These functions are then used with simulated J/ψ decays to estimate the efficiency of the ERT trigger for triggering on e^+e^- pairs from J/ψ decays ($\epsilon_{\rm ERT}^{J/\psi}$). The trigger efficiency is evaluated only for simulated J/ψ decays for which both electrons passed an acceptance and trigger check in order to avoid double counting the acceptance efficiency. This procedure is repeated independently for each of the two EMCal trigger thresholds used during the run. The p_T dependence of $\epsilon_{\rm ERT}^{J/\psi}$ is shown in Fig. 3, where both ERT trigger thresholds have been combined using the relative luminosities of each data sample. It has an average value of 77%. The dip seen at $p_T \approx 3$ GeV/c is due to the kinematics of the J/ψ decays. In that p_T range there is a high probability for the decay electrons to have unbalanced momenta, where one of the electrons will have a momentum below or near the trigger threshold, resulting in a lower probability for triggering on the J/ψ. The effect of the fit function used in the EMCal trigger tile efficiencies is investigated by replacing the error function with a double-Fermi function. This gives an average change in the J/ψ ERT efficiency of 0.31%. The statistical uncertainty in the trigger tile efficiency leads to an uncertainty in the J/ψ ERT efficiency of 1.6%. Summing these uncertainties in quadrature gives a total uncertainty on $\epsilon_{\rm ERT}^{J/\psi}$ of 1.6%, which is heavily dominated by the uncertainty in the efficiency of each ERT trigger tile.

The detector occupancy effect is negligible, even in 0–20% central d+Au collisions (a finding consistent with previous embedding studies in peripheral Cu+Cu [25] with similar multiplicities). A 1% systematic uncertainty was assigned based on studies where simulated J/ψ decays were embedded into real events. This result agrees well with the studies done in [16], where a slightly larger systematic uncertainty was assigned because of the lower statistical precision of the simulations used.

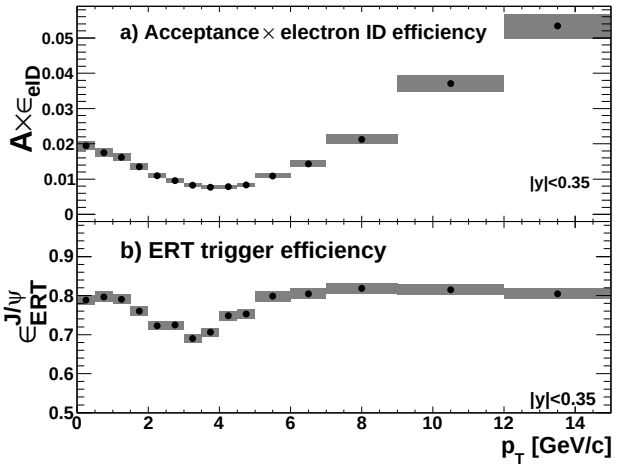

FIG. 3: The J/ψ acceptance × electron ID efficiency (a) and J/ψ ERT trigger efficiency (b) as a function of p_T for $|y| < 0.35$ where the shaded boxes represent the systematic uncertainties.

D. Invariant Yield Results

The J/ψ invariant yield in a given rapidity, transverse-momentum, and centrality bin is

$$\frac{B_{ll}}{2\pi p_T}\frac{d^2N}{dydp_T} = \frac{1}{2\pi p_T \Delta p_T \Delta y}\frac{cN_{J/\psi}}{N_{\rm EVT}\epsilon_{\rm tot}}, \qquad (2)$$

where B_{ll} is the $J/\psi \to l^+l^-$ branching ratio, $N_{J/\psi}$ is the measured J/ψ yield, $N_{\rm EVT}$ is the number of sampled MB events in the given centrality bin, Δy is the width of the rapidity bin, Δp_T is the width of the p_T bin, $\epsilon_{\rm tot} = A \times \epsilon_{\rm eID}\ \epsilon_{\rm ERT}^{J/\psi}\ \epsilon_{\rm rad}$ and c is the BBC bias correction factor described in Sec. II. At midrapidity $N_{J/\psi} = N_{e^+e^-}(1-\epsilon_{\rm cont})$, where $\epsilon_{\rm cont}$ is the correlated dielectron continuum contribution in the J/ψ mass range. The 0–100% centrality integrated J/ψ invariant yield is shown as a function of p_T in Fig. 4, and for four centrality bins in Fig. 5. Here the values shown represent the average over the p_T bin and are plotted at the center of the bin, as this provides the measured information without introducing further systematic uncertainties.

TABLE II: A summary of the systematic uncertainties at $|y| < 0.35$.

Source	Value	Type
Embedding	1.0%	C
$\epsilon_{\rm rad}$	0.2%	C
$\epsilon_{\rm cont}$	0.2%	C
c (Invariant yield only)	0.1–5.8%	C
$c/\langle N_{\rm coll}\rangle$ ($R_{d\rm Au}$ only)	3–6%	C
$A \times \epsilon_{\rm eID}$.	6.5%	B
$\epsilon_{\rm ERT}^{J/\psi}$.	1.6%	B
Stat. Uncertainty on the correlated e^+e^- yield		A

A summary of all the relevant systematic uncertainties at midrapidity is shown in Table II, along with their classification into Type A, B, or C uncertainties. Type A represents uncertainties that are uncorrelated from point to point, Type B represents uncertainties that are correlated from point to point, and Type C represents uncertainties in the overall normalization.

E. p+p Baseline

The p+p baseline used to calculate $R_{d\rm Au}$ is extracted from 2006 data published in [15]. The integrated luminosity was 6.2±0.6 pb^{-1}. In the analysis, described in detail in [15], the effect of the J/ψ polarization on the J/ψ acceptance is included. This effect is not included in the d+Au result presented here due to a lack of knowledge of the effects of a nuclear target on the J/ψ polarization. The J/ψ polarization is therefore assumed to be zero. To remain consistent, this effect is removed from the p+p baseline as well, so that, assuming the polarization does not change drastically between p+p and d+Au, the effects will cancel in the nuclear ratio, $R_{d\rm Au}$. The p+p invariant yields as a function of p_T used in this work, shown in Fig. 4, have been converted from the invariant cross sections published in [15] using an inelastic cross section of 42 mb.

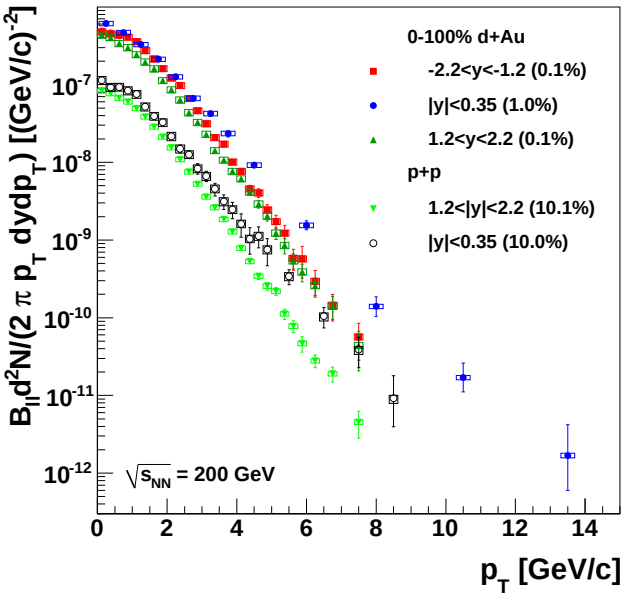

FIG. 4: (Color Online) J/ψ invariant yield as a function of p_T for p+p and 0–100% centrality integrated d+Au collisions. The type C systematic uncertainty for each distribution is given as a percentage in the legend. The midrapidity d+Au and p+p results are discussed in Secs. III D & III E while the forward/backward rapidity results are discussed in Secs. IV C & IV D.

IV. J/ψ ANALYSIS AND RESULTS IN THE FORWARD/BACKWARD RAPIDITY REGION

The procedure for analyzing the $J/\psi \to \mu^+\mu^-$ signal at backward and forward rapidity in the muon arms is discussed in this section. The procedures are similar to those detailed in [15], with only a brief summary presented here, except where there are differences. As in [15], the rapidity region of the forward muon arm used in the analysis was truncated to $1.2 < y < 2.2$ to match the rapidity coverage of the backward muon arm. The extraction of the raw J/ψ yield is discussed in Sec. IV A. The estimation of the detector efficiencies is described in Sec. IV B. The calculation of the J/ψ invariant yield is detailed in Sec. IV C. The p+p baseline used in calculating $R_{d\rm Au}$ is described in Sec.IV D.

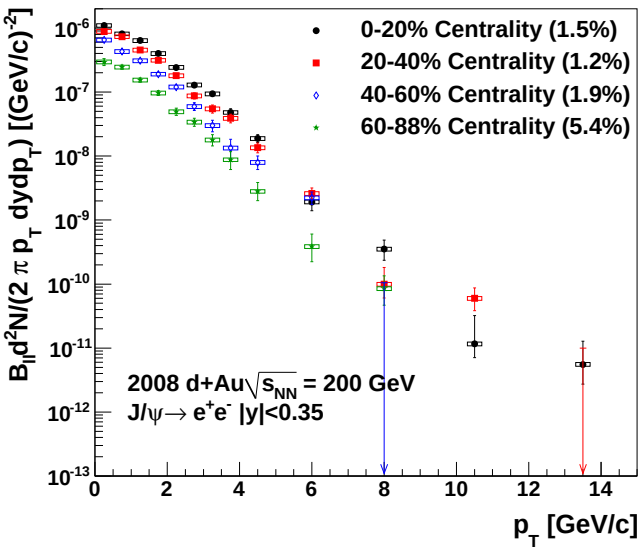

FIG. 5: (Color Online) J/ψ invariant yield as a function of p_T for each centrality at $|y| < 0.35$. The type C systematic uncertainty for each distribution is given as a percentage in the legend.

A. $J/\psi \to \mu^+\mu^-$ Signal extraction

At forward and backward rapidity, the invariant mass distribution is calculated for all unlike-sign dimuons in events that pass the trigger requirements described in Sec. II. The combinatorial background is estimated from the invariant mass distribution formed by pairing unlike-sign muon candidates from different events. This is done to reduce the background statistical uncertainty below what is possible by subtracting like sign pairs from the same event, and is needed because the signal to background present at forward/backward rapidity is smaller than at midrapidity. The mixed event muon pairs are required to have vertices that differ by no more than 3 cm in the beam direction. The mixed event spectrum is normalized by the factor

$$\alpha = \frac{\sqrt{(N^{\rm same}_{\mu^+\mu^+})(N^{\rm same}_{\mu^-\mu^-})}}{\sqrt{(N^{mixed}_{\mu^+\mu^+})(N^{mixed}_{\mu^-\mu^-})}}, \qquad (3)$$

where $N^{\rm same}_{\mu\mu}$ and $N^{mixed}_{\mu\mu}$ are the number of pairs formed from two muons in the same or in mixed events, respectively.

The remaining correlated dimuon mass distribution after the subtraction of the mixed event combinatorial background contains dimuons from J/ψ and ψ' decays, as well as correlated dimuons from heavy-flavor decays and Drell-Yan pairs. Due to the momentum resolution of the detector, there is no clean discrimination between the J/ψ and ψ' in the mass distribution. However the ψ' contribution is expected to be negligible in the mass window of interest.

A function consisting of an exponential component combined with two Gaussian distributions, which are used to better reproduce the mass resolution present in the muon arms, was used to fit the dimuon mass distribution, convolved with a function to account for the variation in acceptance over the invariant mass range. An example of the fitted mass distribution is shown in Fig. 6. Both the J/ψ component of the fit, and direct counting after the subtraction of the fitted exponential background, are used to evaluate the J/ψ yield. The difference between the two methods is taken as a Type A systematic uncertainty. This uncertainty is typically small ($\approx 2\%$) but can be significantly larger at high p_T where there are fewer counts. Measured J/ψ yields of approximately 38000 and 42000 are obtained at backward and forward rapidity, respectively.

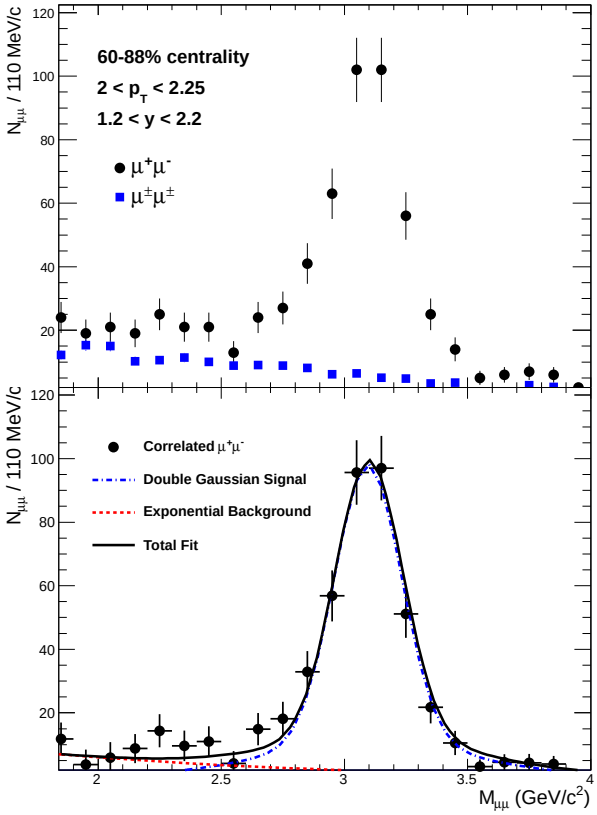

FIG. 6: (Color Online) (top) Invariant mass distribution of unlike-sign (filled circles) and like-sign (filled boxes) dimuon pairs for $2 < p_T < 2.25$ GeV/c at forward rapidity and 60–88% central events. (bottom) Invariant mass distribution of correlated dimuon pairs after the subtraction of the combinatorial background. The solid line represents the fit to the invariant mass distribution, which includes the double Gaussian signal component (dot-dashed line) and exponential background (dotted line).

B. Acceptance and Efficiency Studies

Studies of the response of the muon arm spectrometers to dimuons from J/ψ decays are performed using a tuned GEANT3-based simulation of the muon arms, coupled with a MuID trigger emulator. The MuID panel-by-panel efficiencies are estimated using the fraction of reconstructed roads in real data. Where statistics are limited, the operational history of each channel recorded during the run was used to estimate the efficiency. A systematic uncertainty of 4% is assigned to the MUID efficiency based on this comparison. Charge distributions in each part of the MuTr observed in real data, along with dead channels and their variation with time over the run, are used to give an accurate description of the MuTr efficiency within the detector simulation.

The J/ψ acceptance $\times$ efficiency ($A\times\epsilon$) evaluation uses a PYTHIA simulation with several parton distributions as input to account for the unknown underlying rapidity dependence of the J/ψ yield. A 4% systematic uncertainty is assigned based on changes in the input parton distributions. A systematic uncertainty of 6.4(7)% on the J/ψ yield is assigned to the backward(forward) rapidity due to the uncertainties in the acceptance x efficiency determination method itself.

C. Invariant Yield Results

TABLE III: The dominant systematic errors at $1.2 < |y| < 2.2$.

Source	Value (S/N)	Type
c (Invariant yield only)	0.1-5.8%	C
$c/\langle N_{\rm coll}\rangle$ ($R_{d\rm Au}$ only)	3-6%	C
MC Input Distributions.	4%	B
MuTr Efficiency	2%	B
MUID Efficiency	4%	B
Acceptance	6.4/7%	B
Fit Type	≈ 2%	A
Stat. Uncertainty on the measured J/ψ yield		A

The J/ψ invariant yield at backward/forward rapidity is calculated using Eq. 2, where $\epsilon_{\rm tot} = A\times\epsilon$. A summary of the systematic uncertainties is given in Table III. The backward and forward 0–100% centrality-integrated J/ψ invariant yields are shown as a function of p_T in Fig. 4, while the J/ψ invariant yields are shown as a function of p_T in each centrality bin in Fig. 7.

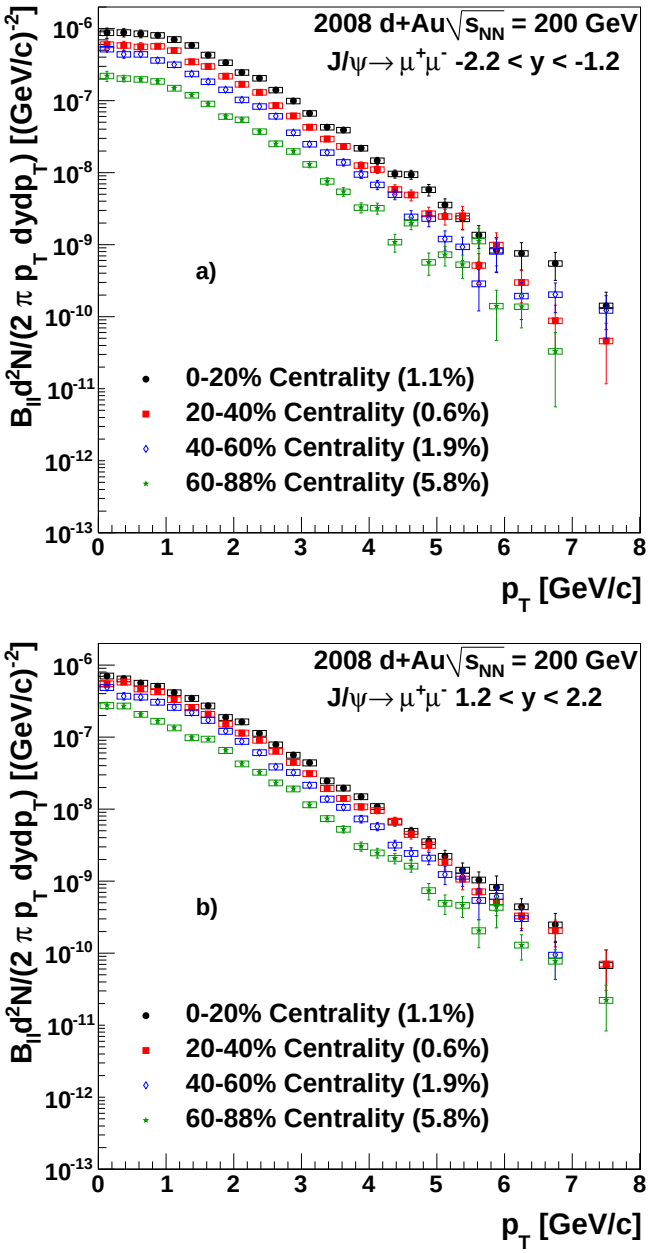

FIG. 7: (Color Online) J/ψ invariant yield as a function of p_T for each centrality for a) $-2.2 < y < -1.2$ and b) $1.2 < y < 2.2$. The type C systematic uncertainty for each distribution is given as a percentage in the legend.

D. p+p Baseline

The p+p baseline used to calculate $R_{d\rm Au}$ is extracted from a combined analysis of data taken in 2006 and 2008, published in [15]. The combined integrated luminosity was 9.3±0.9 pb^{-1}. As discussed in Sec. III E, the effect of the J/ψ polarization on the J/ψ acceptance is removed from the results used here. The J/ψ invariant yield in p+p collisions at forward/backward rapidity used here is shown as a function of p_T in Fig. 4 for convenience,

where we have converted from the invariant cross sections published in [15] using an inelastic cross section of 42 mb.

V. CALCULATION OF $\langle P_T^2 \rangle$

The $\langle p_T^2 \rangle$ is calculated for each of the J/ψ invariant yields presented in Secs. III D and IV C, and the resulting values are shown in Table IV.

TABLE IV: $\langle p_T^2 \rangle$ results for p+p and d+Au collisions where the first quoted uncertainty corresponds to the type A uncertainties and the second corresponds to the type B uncertainties.

System	y range	Centrality	$\langle p_T^2 \rangle$ [GeV$^2/c^2$]
p+p	$1.2 < \|y\| < 2.2$		3.64±0.03±0.06
p+p	$\|y\| < 0.35$		4.46±0.14±0.18
d+Au	$-2.2 < y < -1.2$	0–100%	4.09±0.06±0.09
d+Au	$\|y\| < 0.35$	0–100%	$5.10^{+0.12}_{-0.10}$±0.11
d+Au	$1.2 < y < 2.2$	0–100%	4.05±0.05±0.10
d+Au	$-2.2 < y < -1.2$	0–20%	4.22±0.08±0.09
d+Au	$-2.2 < y < -1.2$	20–40%	4.06±0.08±0.09
d+Au	$-2.2 < y < -1.2$	40–60%	4.01±0.09±0.09
d+Au	$-2.2 < y < -1.2$	60–88%	3.92±0.10±0.09
d+Au	$\|y\| < 0.35$	0–20%	$5.24^{+0.19}_{-0.16}$±0.10
d+Au	$\|y\| < 0.35$	20–40%	$5.27^{+0.22}_{-0.19}$±0.12
d+Au	$\|y\| < 0.35$	40–60%	$5.08^{+0.29}_{-0.26}$±0.16
d+Au	$\|y\| < 0.35$	60–88%	$4.60^{+0.30}_{-0.24}$±0.15
d+Au	$1.2 < y < 2.2$	0–20%	4.15±0.06±0.10
d+Au	$1.2 < y < 2.2$	20–40%	4.13±0.07±0.11
d+Au	$1.2 < y < 2.2$	40–60%	3.94±0.07±0.10
d+Au	$1.2 < y < 2.2$	60–88%	3.80±0.08±0.10

Unlike in previous analyses [16], where the $\langle p_T^2 \rangle$ was calculated for $p_T \leq 5$ GeV/c due to statistical limitations at high p_T, here we have calculated the $\langle p_T^2 \rangle$ over the full p_T range. First the $\langle p_T^2 \rangle$ was calculated numerically up to the p_T limits of the measured distribution $\left(\langle p_T^2 \rangle|_{p_T \leq p_T^{\max}}\right)$. The correlated uncertainty was propagated to $\langle p_T^2 \rangle|_{p_T \leq p_T^{\max}}$ by sampling the type B uncertainty distributions of the first and last p_T point of the invariant yield, and assuming a linear correlation in between. For a more detailed description of this procedure see Appendix A 3.

To account for the differences in the p_T limits of the various distributions, the $\langle p_T^2 \rangle|_{p_T \leq p_T^{\max}}$ value was corrected to the p_T range from zero to infinity. This was done by fitting the distribution with a modified Kaplan function of the form

$$f(p_T) = p_0 \left(1 - \left(\frac{p_T}{p_1}\right)^2\right)^{p_2} \quad (4)$$

where each parameter was free to vary. The ratio

$$k = \frac{\langle p_T^2 \rangle[0, \infty]}{\langle p_T^2 \rangle[0, {p_T}^{\max}]} \quad (5)$$

was then calculated from the fit and applied to the numerically calculated $\langle p_T^2 \rangle|_{p_T \leq p_T^{\max}}$. In all cases the correction factor was small ($k < 1.03$), and an uncertainty in the correction factor based on the fit uncertainty is included in the Type B uncertainties shown in Table IV. For a more detailed description of this procedure, including the fit results and the calculated values of k see Appendix A.

The $\langle p_T^2 \rangle$ for p+p collisions was previously published in [15]. But we report the result here with the effect of the J/ψ polarization on the acceptance removed. The results are in good agreement with those presented in [15], and are shown in Table IV.

Figure 8 shows $\Delta\langle p_T^2 \rangle = \langle p_T^2 \rangle_{dAu} - \langle p_T^2 \rangle_{pp}$ as a function of $N_{\rm coll}$. There is a broadening in the p_T distribution with respect to p+p, which increases with $N_{\rm coll}$, and is similar at forward and backward rapidities. We observe a larger increase in the p_T broadening at midrapidity. However, this observation is tempered by the relatively large uncertainties present in the data.

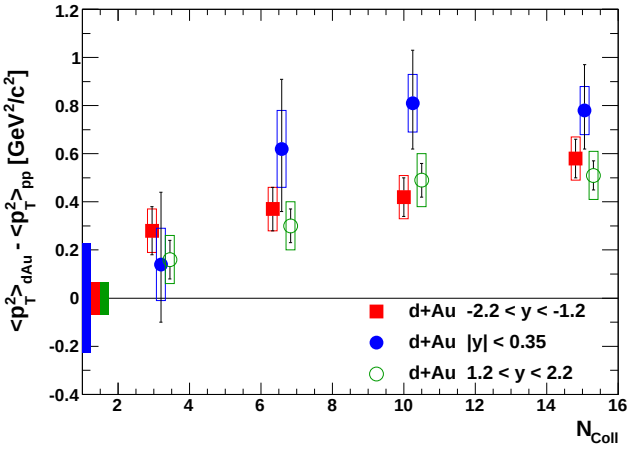

FIG. 8: (Color Online) The difference between the J/ψ $\langle p_T^2 \rangle$ in d+Au and p+p collisions as a function of $N_{\rm coll}$ in d+Au collisions. The boxes drawn at $\Delta\langle p_T^2 \rangle = 0$ represent the combined statistical and systematic uncertainties from the p+p calculation.

VI. THE J/ψ $R_{d\rm Au}$

To quantify the d+Au cold nuclear matter effects, the J/ψ $R_{d\rm Au}$ is calculated for a given p_T, y, and centrality

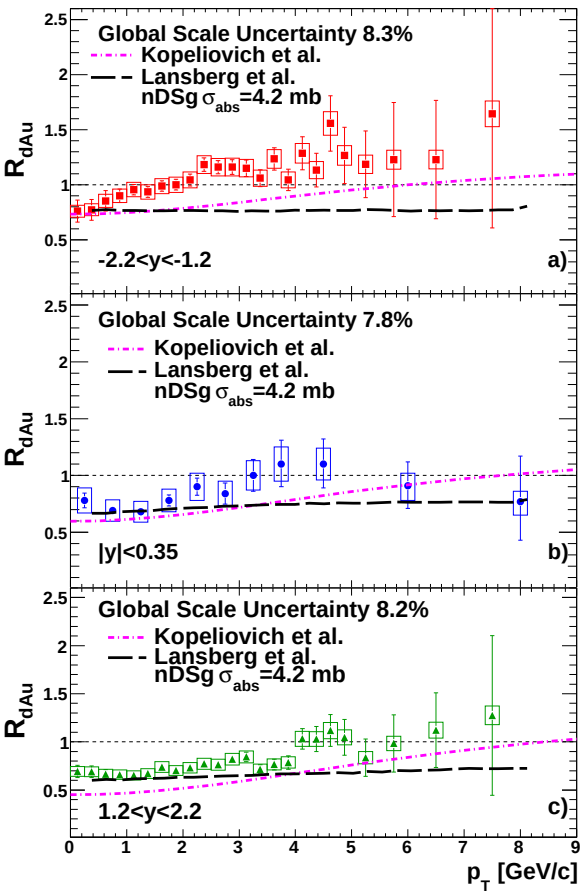

FIG. 9: (Color Online) J/ψ nuclear modification factor, $R_{d\mathrm{Au}}$, as a function of p_T for (a) backward rapidity, (b) midrapidity, and (c) forward rapidity 0–100% centrality integrated d+Au collisions. Curves are model calculations detailed in Sec. VI A.

bin as:

$$R_{d\mathrm{Au}}(i) = \frac{c}{\langle N_{\mathrm{coll}}(i)\rangle} \frac{d^2N^{d+\mathrm{Au}}_{J/\psi}(i)/dydp_T}{d^2N^{p+p}_{J/\psi}/dydp_T}, \qquad (6)$$

where $d^2N^{d+\mathrm{Au}}_{J/\psi}(i)/dydp_T$ is the d+Au invariant yield for the i^{th} centrality bin, $d^2N^{p+p}_{J/\psi}/dydp_T$ is the p+p invariant yield for the same p_T and y bin, and $\langle N_{\mathrm{coll}}(i)\rangle$ is the average number of binary collisions for the given centrality bin, as listed in Table I.

The 0–100% centrality integrated J/ψ $R_{d\mathrm{Au}}$ as a function of p_T is shown in Fig. 9 for each of the three rapidity regions. The numerical values can be found in Table VII, VIII, and IX for backward, mid and forward rapidity, respectively. Figure 9 shows a different behavior for $R_{d\mathrm{Au}}$ at backward ($-2.2 < y < -1.2$) as opposed to mid ($|y| < 0.35$) and forward ($1.2 < y < 2.2$) rapidities. At backward rapidity, the $R_{d\mathrm{Au}}$ is suppressed only at the lowest p_T, with a rapid increase to $R_{d\mathrm{Au}} = 1.0$ at $p_T \approx 1.5$ GeV/c . The mid and forward rapidity data, on the other hand, exhibit a similar level of suppression at the lowest p_T, but a much more gradual increase in $R_{d\mathrm{Au}}$ with p_T, increasing to $R_{d\mathrm{Au}} = 1.0$ only at $p_T \approx 4.0$ GeV/c . Figure 10 shows the same 0–100% $R_{d\mathrm{Au}}$ vs p_T at all rapidities overlaid. It is striking that the shape and absolute scale for the mid and forward rapidity data is nearly consistent across the entire p_T range of the data.

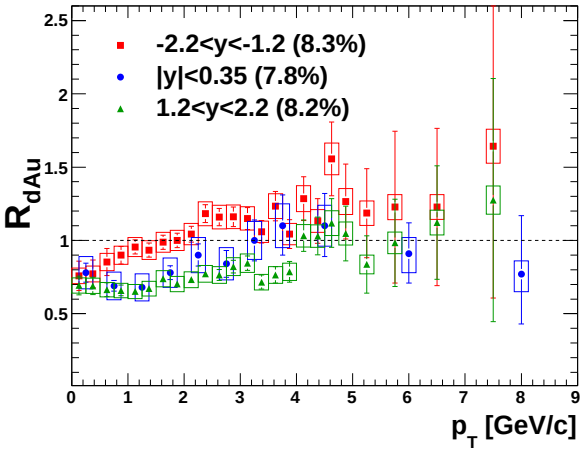

FIG. 10: (Color Online) J/ψ $R_{d\mathrm{Au}}$, as a function of p_T for 0–100% centrality integrated d+Au collisions at each rapidity. The Type C systematic uncertainty for each distribution is given as a percentage in the legend.

Due to the statistical limitations of the data at high p_T, it is unclear from Fig. 9 whether the $R_{d\mathrm{Au}}$ increases significantly above one. To investigate the high-p_T behavior of the $R_{d\mathrm{Au}}$ at each rapidity, the average $R_{d\mathrm{Au}}$ was calculated for $p_T > 4$ GeV/c by fitting each distribution with a constant. The results are shown in Table V along with the fit uncertainties, which take into account only the type A uncertainties on the data. Since the type B uncertainties are roughly consistent in the fit range, we have chosen here to add the average type B uncertainty for $p_T > 4$ GeV/c in quadrature with the type C uncertainty. We find that at mid and forward rapidity the average $R_{d\mathrm{Au}}$ for $p_T > 4$ GeV/c is consistent with 1.0, while at backward rapidity the average $R_{d\mathrm{Au}}$ is greater than 1.0.

The production of a J/ψ at forward rapidity in $A + A$ collisions involves a low-x gluon colliding with a high-x gluon. The symmetry due to identical colliding nuclei results, essentially, in the folding of the forward and backward rapidity $R_{d\mathrm{Au}}$. The production of a J/ψ at midrapidity results, essentially, in the folding of the midrapidity $R_{d\mathrm{Au}}$ with itself. This picture is simplistic and leaves out many details, but it gives some expectation for the result of the modification of J/ψ production in $A + A$ collisions due to CNM effects. If we extrapolate the observed behavior of $R_{d\mathrm{Au}}$ to the modification of J/ψ's produced at forward rapidity in $A + A$ collisions, we would expect a R_{AA} contribution from CNM effects to be similar to, or greater than, 1.0 at high p_T and a modification similar to 1.0 at midrapidity. The observation at midra-

pidity of a J/ψ $R_{\rm AA}$ in Cu+Cu collisions that exceeds, but is consistent with, 1.0 at high p_T [26] may therefore be largely accounted for by the contribution from CNM effects. Further work is needed to understand the detailed propagation of measured results in d+Au collisions to an expected CNM contribution in A+A collisions before this can be fully understood.

TABLE V: The average 0–100% $R_{d\rm Au}$ for $p_T > 4$ GeV/c where the first quoted uncertainty corresponds to the fit uncertainty and the second corresponds to the combined type B and C systematic uncertainties.

Rapidity	$R_{d\rm Au}$ ($p_T > 4$ GeV/c)
$-2.2 < y < -1.2$	1.27±0.06±0.11
$\|y\| < 0.35$	0.97±0.14±0.16
$1.2 < y < 2.2$	1.03±0.06±0.11

Figures 11, 12, and 13 show $R_{d\rm Au}$ vs p_T in four centrality bins for backward rapidity, midrapidity, and forward rapidity, respectively. Numerical values can be found in Tables X, XI, XII and XIII for 0–20%, 20–40%, 40–60% and 60–88% central collisions respectively. For peripheral collisions the $R_{d\rm Au}$ remains consistent with 1.0 within statistical and systematic uncertainties across all p_T in all rapidity regions.

A. Comparison with Model Predictions

As mentioned previously, various models have been suggested to describe the cold nuclear matter effects on J/ψ production. The models that will be discussed here include a combination of physical effects such as shadowing, nuclear breakup, and the Cronin effect.

Shadowing, the modification of the parton distributions within a nucleus, is calculated using parametrizations of deep inelastic scattering data in the form of nuclear modified parton distribution functions (nPDF's). There are a number of nPDF sets available, including nDSg [28], EKS98 [29] and EPS09 [30], which provide distributions of this modification based on different parametrizations of the available data. For J/ψ production in d+Au collisions the relevant distributions are those providing the modification of the gluon distribution within a Au nucleus, as J/ψ's are produced primarily through gluon fusion at $\sqrt{s_{NN}}$ =200 GeV. The nPDF's provide modifications as a function of parton momentum fraction (x) and energy transfer (Q^2). Knowledge of the J/ψ production kinematics is then needed to produce a modification to J/ψ production in d+Au collisions. For J/ψ production at backward rapidity and $0 < p_T < 8$ GeV/c , a range of roughly $0.051 < x < 0.39$ in the Au nucleus is probed, assuming simple 2→1 kinematics. While 2→1 kinematics are inadequate to describe the production of a J/ψ with nonzero p_T, they are used here to provide a simple estimation of the x and Q^2 ranges covered. Likewise, midrapidity covers roughly $0.0094 < x < 0.071$ and forward rapidity covers roughly $0.0017 < x < 0.013$. A range of roughly $10 < Q^2[\mathrm{GeV}^2/c^2] < 74$ is probed at each rapidity under the same assumptions. The data thus provide a strong constraint to shadowing models over a wide range of x and Q^2.

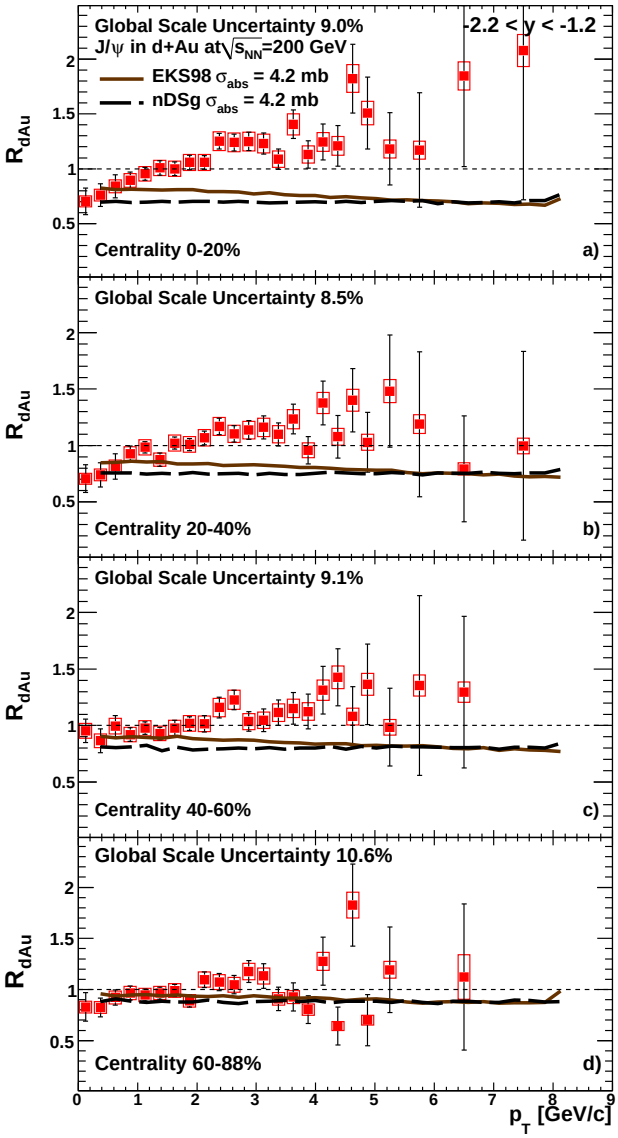

FIG. 11: (Color Online) $J/\psi \to \mu^+\mu^-$ $R_{d\rm Au}$, as a function of p_T for a) central, b) midcentral, c) midperipheral, and d) peripheral events at $-2.2 < y < -1.2$. The 60–88% $R_{d\rm Au}$ point at $p_T = 5.75$ GeV/c has been left off the plot, as it is above the plotted range and has very large uncertainties, however it is included in Table XIII. Curves are calculations by Lansberg et al. [27] discussed in the text.

Nuclear breakup, the dissociation of $c\bar{c}$ pairs that would have formed J/ψ's through collisions with nucleons, is often parametrized through a breakup cross section. Little theoretical or experimental guidance cur-

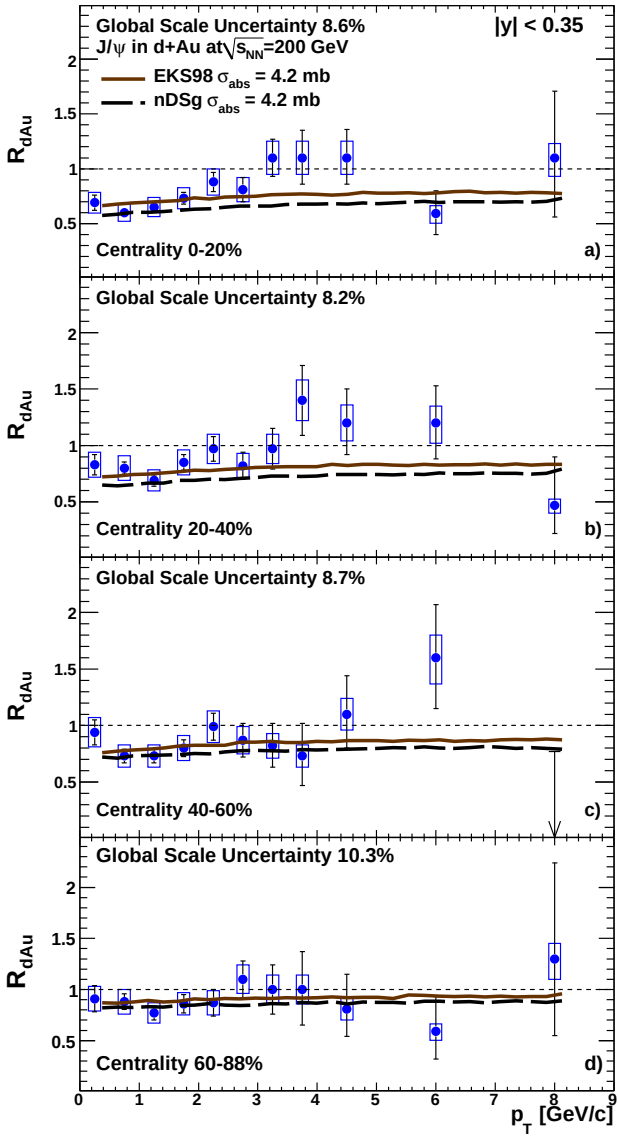

FIG. 12: (Color Online) $J/\psi \to e^+e^-$ $R_{d\mathrm{Au}}$, as a function of p_T for a) central, b) midcentral, c) midperipheral, and d) peripheral events at $|y| < 0.35$. Curves are calculations by Lansberg et al. [27] discussed in the text.

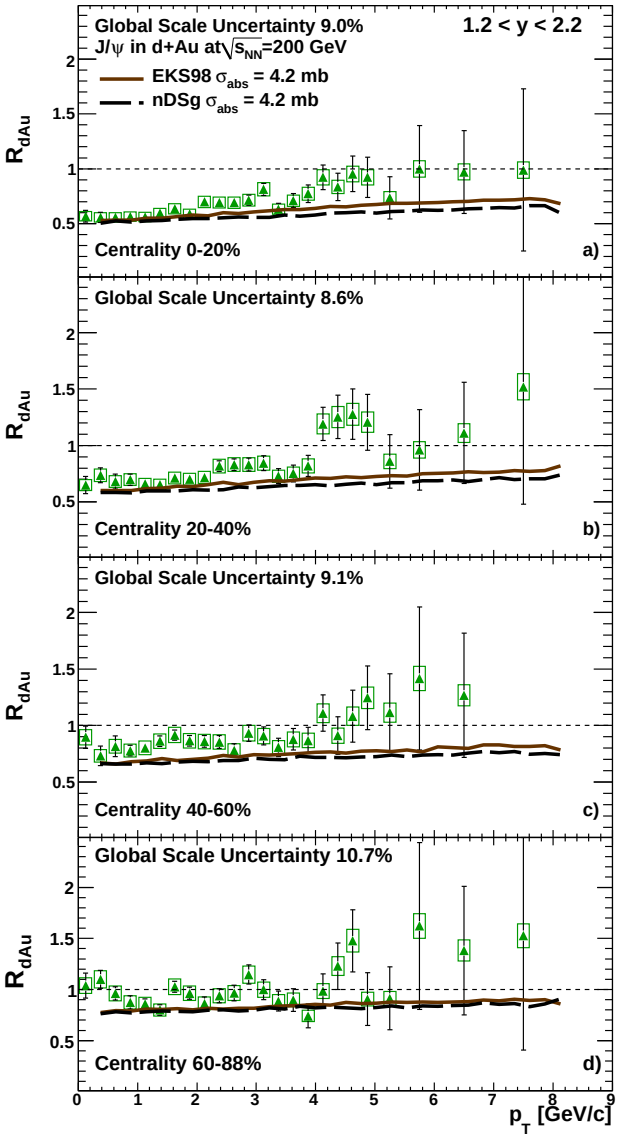

FIG. 13: (Color Online) $J/\psi \to \mu^+\mu^-$ $R_{d\mathrm{Au}}$, as a function of p_T for a) central, b) midcentral, c) midperipheral, and d) peripheral events at $1.2 < y < 2.2$. Curves are calculations by Lansberg et al. [27] discussed in the text.

rently exists on the exact nature of this effect due to the many complications and competing effects involved in J/ψ production in $p(d)+A$ collisions. Often this effect is modeled by a simple "effective" cross section, which remains constant with p_T, however there are a number of models, including a dynamic breakup cross section that changes based on the kinematics of the produced J/ψ.

The broadening of the p_T distribution, termed the Cronin effect [31], is typically attributed to multiple elastic scattering of the incoming parton before the hard collision that produces the J/ψ. This modifies the p_T dependence of the J/ψ production by adding p_T vectorially to the incoming parton. This generally causes a decrease in J/ψ production at low p_T and a compensating increase at higher p_T ($p_T \approx 5-10$ GeV/c), which eventually falls off at yet higher p_T ($p_T \approx 10$ GeV/c).

The first set of model calculations that we discuss is by Kopeliovich et al. [32, 33] calculates the effects on a $c\bar{c}$ dipole propagating through a nucleus. The J/ψ production is calculated based on 2→1 kinematics,

$$x = \frac{\sqrt{\langle M^2_{c\bar{c}}\rangle + \langle {p_T}^2\rangle}}{\sqrt{s}} e^{-y}, \qquad (7)$$

where $\langle M^2_{c\bar{c}}\rangle = 2M^2_{J/\psi}$ is fixed based on the $c\bar{c}$ invariant mass distribution predicted by the color singlet model. The calculation includes shadowing, taken from the nDSg nPDF set, as well as nuclear breakup and the

Cronin effect. The nuclear breakup is calculated using a parametrization of the dipole cross section fitted to measurements of the proton structure function at HERA [34], yielding a breakup cross section that is dependent on kinematics of the J/ψ. The results from this calculation are shown for the 0–100% $R_{d\mathrm{Au}}$ at all rapidities in Fig. 9 as the dot-dashed curves. This is a parameter free calculation, with no overall normalization or fits to the data presented here. The p_T shape is in good agreement with the data at mid and forward rapidity, but the theory shows a greater overall level of suppression than is seen in the data. At backward rapidity there is a disagreement with the shape of the p_T distribution. While the theory predicts a similar p_T shape at all rapidities, the data show a much faster rise in $R_{d\mathrm{Au}}$ with increasing p_T at backward rapidity. It is also worth noting, as shown in [35], that this model cannot simultaneously describe the rapidity dependence of the PHENIX $R_{d\mathrm{Au}}$ and R_{CP}, which is the ratio of $R_{d\mathrm{Au}}$ in central collisions to the $R_{d\mathrm{Au}}$ in peripheral collisions, for J/ψ production and therefore may not have an accurate description of the geometric dependence of the modification.

A second set of model calculations, performed by Lansberg et al. [27, 36], are shown in Figure 9. This model uses a Monte-Carlo approach within a Glauber model of d+Au collisions. The J/ψ production is calculated using the color singlet model that utilizes $2 \rightarrow 2$ kinematics, namely $g + g \rightarrow J/\psi + g$, where the majority of the J/ψ p_T is balanced by the emission of a hard gluon in the final state, rather than $2 \rightarrow 1$ processes, where the J/ψ p_T comes entirely from the transverse momentum carried by the colliding gluons. The J/ψ production is modified in d+Au collisions by shadowing effects parametrized using various nPDF sets. The calculations shown in Fig. 9 utilize the nDSg nPDF set. Similar calculations using the EKS98 and EPS08 [37] nPDF sets can be found in [27]. Nuclear breakup of the J/ψ is taken into account through the use of an effective, p_T-independent, absorption cross section of 4.2 mb. Results using σ_{abs} =0, 2.6, and 6 mb can also be found in [27]. We have chosen to highlight only $\sigma_{abs} = 4.2$ mb here as it reproduces the rapidity dependence of the 60–88% $R_{d\mathrm{Au}}$ reasonably well [27] where shadowing corrections are expected to be small. The results of this calculation, shown in Fig. 9 for 0–100% $R_{d\mathrm{Au}}$ at all rapidities, shows reasonable agreement with the overall level of modification seen at low p_T in the data at mid and forward rapidities while the calculation predicts a flatter distribution with increasing p_T than is seen in the data. The shape of the distribution at backward rapidity is markedly different than the data. While the data rapidly increase to $R_{d\mathrm{Au}} \approx 1$ at low p_T, the calculation shows a $R_{d\mathrm{Au}}$ that is essentially constant with increasing p_T.

When comparing the two sets of model calculations in Fig. 9 the calculations from Kopeliovich et al. [32, 33] have a different and more pronounced shape when compared to the calculations from Lansberg, et al [27, 36]. Both sets of calculations utilize the nDSg nPDF set, suggesting a common contribution from shadowing. However, the J/ψ production kinematics are calculated differently, which will lead to some difference in the shadowing contribution. The calculations from Kopeliovich et al. include the Cronin effect, which provides a decrease in J/ψ production at low p_T and an increase at higher p_T, creating an $R_{d\mathrm{Au}}$ that exhibits less suppression at high p_T than at low p_T. The calculations from Lansberg et al. do not include the Cronin effect, and therefore the p_T shape of $R_{d\mathrm{Au}}$ should be dominated by the effect of shadowing, and therefore the choice of nPDF set.

The spatial dependence of the shadowing has been taken into account in [27], where it is assumed that the shadowing is proportional to the local density. This assumption allows for calculation of the $R_{d\mathrm{Au}}$ vs p_T in different centrality bins. The results of the calculation in the four PHENIX centrality bins are shown in Figures 11, 12 and 13 for backward, mid, and forward rapidity, respectively. Here we have chosen to include calculations using the EKS98 nPDF set along with those using the nDSg nPDF set as this will provide a direct comparison between the effects due to different nPDF sets, since the J/ψ production kinematics and σ_{abs} values are identical between the two calculations. At mid and forward rapidity the calculations are similar to each other and show reasonable agreement with the $R_{d\mathrm{Au}}$ distributions within the current statistical and systematic uncertainties, although the calculation appears to predict a slightly larger average suppression for peripheral collisions at forward rapidity than is seen in the data. This could be due to the value of σ_{abs} used at forward rapidity, as the value of 4.2 mb was chosen by eye rather than fitted to the data, and it may not be independent of y.

At backward rapidity the calculations are in disagreement with the data for all but the most peripheral collisions, where both the calculations and the data show an $R_{d\mathrm{Au}}$ consistent with 1.0 at all p_T. While the calculations at backward rapidity using the nDSg nPDF set are roughly constant with p_T for each centrality, the calculations using the EKS98 nPDF set show an enhancement in the suppression of $R_{d\mathrm{Au}}$ with increasing p_T for central and midcentral collisions, whereas the data shows the opposite trend. At backward rapidity and low p_T (Bjorken $x \approx 0.1$ for the parton in the Au nucleus) production occurs in the anti-shadowing region, while at high p_T ($x \approx 0.3$) production begins to move towards what is termed the EMC [38] region. In 1986, a suppression of the quark distributions within nuclei was discovered in the range $0.35 < x < 0.7$ by the European Muon Collaboration (EMC) [38] in deep inelastic scattering. While there is still debate about the source of this suppression in the quark distributions, no direct evidence of an EMC effect has yet been reported in the gluon distributions. Few constraints exist in this region, and there is large disagreement in the modification of the gluon density between nPDF's. The nDSg nPDF set includes no suppression in the EMC region, and only a small anti-shadowing effect, while the EKS98 nPDF exhibits a sup-

pression in the EMC region similar to that observed in the quark distributions, and a larger anti-shadowing effect (see [30] for a comparison of nPDF sets). The larger anti-shadowing combined with the inclusion of an EMC effect in the EKS98 nPDF set cause a decrease in the calculated $R_{d\mathrm{Au}}$ as p_T (and correspondingly, x) increases. The lack of a strong anti-shadowing effect combined with the absence of an EMC effect in the nDSg nPDF causes the calculation of $R_{d\mathrm{Au}}$ to remain roughly constant with increasing p_T.

In [39] the authors infer from measurements of Υ production at RHIC that a strong EMC effect must be present to explain the observed modification. Depending on the mapping of the J/ψ y and p_T to x, which is model dependent, the high p_T data at backward rapidity may allow us to probe this region. The large uncertainties present in the high p_T $R_{d\mathrm{Au}}$, along with complications from competing physics effects in this region, however, prevent any strong conclusions from being drawn at this time.

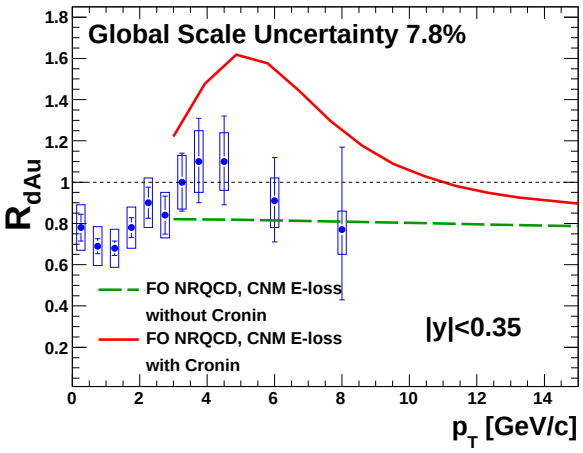

FIG. 14: (Color Online) J/ψ $R_{d\mathrm{Au}}$, as a function of p_T momentum for midrapidity 0–100% centrality integrated d+Au collisions. The curves are theoretical calculations from [40] described in the text.

A third set of model calculations by Sharma and Vitev [40] is compared with the midrapidity 0–100% centrality integrated $R_{d\mathrm{Au}}$ in Fig. 14. This model describes J/ψ production using nonrelativistic quantum chromodynamics (NRQCD). The effect of nuclear shadowing is calculated using EKS98 in the EMC region ($x > 0.25$), while for lower values, power suppressed coherent final-state scattering leads to a modification of parton x [41]. Initial state energy loss, which accounts for the radiative energy loss of the incoming particles through multiple interactions with the target nucleus is included. This effect reduces the energy of the incoming parton, so, to achieve the same final-state kinematics the parton must have a greater momentum, and therefore a larger value of x. This effectively shifts the portion of the gluon distribution sampled to higher x. Also included is a calculation of the Cronin effect. The solid curve in Fig. 14 shows the full calculation including the Cronin effect. The dashed curve in Figure 14 is the same calculation without the Cronin effect. This comparison gives a direct indication of the contribution from the Cronin effect, which is evidently over predicted when compared to the data. The results presented here will hopefully provide a much needed constraint on the Cronin effect at RHIC energies. The calculation including the Cronin effect indicate an $R_{d\mathrm{Au}}$ that decreases at higher p_T. This is consistent with data, however the current statistical and systematic uncertainties make determining the precise trend of $R_{d\mathrm{Au}}$ difficult at high p_T. Better data with a larger p_T coverage is needed to determine the J/ψ modification at higher p_T.

VII. SUMMARY & CONCLUSIONS

We have measured the J/ψ invariant yield and $R_{d\mathrm{Au}}$, as a function of p_T over three rapidity ranges in d+Au collisions at $\sqrt{s_{NN}} = 200$ GeV using the PHENIX detector. These measurements provide a large improvement in statistical precision and p_T reach over the previously published PHENIX d+Au results [16, 17], and are the first measurements of the centrality dependence of the J/ψ p_T distribution in d+Au collisions by PHENIX. The $\Delta\langle p_T^2\rangle$ values determined from the data show a marked increase with N_{coll} that is similar at all rapidities.

The $R_{d\mathrm{Au}}$ vs p_T displays similar behavior at mid and forward rapidity, showing suppression at low p_T with a gradual increase to a value consistent with 1.0. The $R_{d\mathrm{Au}}$ at backward rapidity has a different distribution with p_T, showing a more rapid increase from suppression to a value of 1.0, and transitioning to $R_{d\mathrm{Au}} > 1.0$ above 2 GeV/c . These trends are greater for central collisions, while the peripheral collisions show $R_{d\mathrm{Au}}$ consistent with 1.0 across all rapidities.

We find an average $R_{d\mathrm{Au}}$ for $p_T > 4$ GeV/c of $1.27 \pm 0.06 \pm 0.11$ at backward rapidity, and an $R_{d\mathrm{Au}}$ consistent with 1.0 at mid and forward rapidity. This implies a CNM contribution in $A + A$ collisions that is likely consistent with 1.0 at high p_T across all rapidity. This could potentially explain the reported increase in R_{AA} with increasing p_T [26]. However more data and further work to understand the propagation of $R_{d\mathrm{Au}}$ to R_{AA} is needed to confirm this.

A comparison of the measured $R_{d\mathrm{Au}}$ with three types of theoretical calculations was shown. The parameter independent dipole model of J/ψ production in $p + A$ collisions agrees well with the shape of the data at mid and forward rapidities, while the shape of the predicted p_T dependence is different from the data at backward rapidity. However the suppression is over-predicted at all rapidities. The second model uses $2 \to 2$ J/ψ production kinematics coupled with shadowing taken from both EKS98 and nDSg nPDF sets as well as an effective absorption cross section of 4.2 mb. The calculations with

both EKS98 and nDSg show good agreement with the data at midrapidity in each centrality bin, as well as the centrality integrated case. At forward rapidity the shape of the distribution is in reasonable agreement with the data, while the overall level of suppression seems to be greater in the model calculations than the data. At backward rapidity, the model calculations using both EKS98 and nDSG nPDF sets are in strong disagreement with the data. At backward rapidity calculations using the nDSg nPDF set show a suppression that is constant with p_T, while those using the EKS98 nPDF set predict an increase of suppression with increasing p_T. The data show the opposite trend. The third model, an NRQCD calculation of high p_T J/ψ production show a Cronin effect, which although generally consistent with the data, is significantly larger than observed in the data, and a suppression at high p_T that cannot be confirmed due to the large uncertainties at high p_T and the limited p_T reach of the current data.

In summary, the data presented here cover a large range in x and Q^2, providing a further constraint on the modification of the gluon distribution in nuclei, as well as providing constraints on the size of the Cronin effect on J/ψ production at RHIC.

ACKNOWLEDGMENTS

We thank the staff of the Collider-Accelerator and Physics Departments at Brookhaven National Laboratory and the staff of the other PHENIX participating institutions for their vital contributions. We thank Jean-Philippe Lansberg, Nicolas Matagne, Boris Kopeliovich, Ivan Vitev, and Rishi Sharma for useful discussions and theoretical calculations. We acknowledge support from the Office of Nuclear Physics in the Office of Science of the Department of Energy, the National Science Foundation, Abilene Christian University Research Council, Research Foundation of SUNY, and Dean of the College of Arts and Sciences, Vanderbilt University (U.S.A), Ministry of Education, Culture, Sports, Science, and Technology and the Japan Society for the Promotion of Science (Japan), Conselho Nacional de Desenvolvimento Científico e Tecnológico and Fundação de Amparo à Pesquisa do Estado de São Paulo (Brazil), Natural Science Foundation of China (P. R. China), Ministry of Education, Youth and Sports (Czech Republic), Centre National de la Recherche Scientifique, Commissariat à l'Énergie Atomique, and Institut National de Physique Nucléaire et de Physique des Particules (France), Ministry of Industry, Science and Tekhnologies, Bundesministerium für Bildung und Forschung, Deutscher Akademischer Austausch Dienst, and Alexander von Humboldt Stiftung (Germany), Hungarian National Science Fund, OTKA (Hungary), Department of Atomic Energy and Department of Science and Technology (India), Israel Science Foundation (Israel), National Research Foundation and WCU program of the Ministry Education Science and Technology (Korea), Ministry of Education and Science, Russian Academy of Sciences, Federal Agency of Atomic Energy (Russia), VR and the Wallenberg Foundation (Sweden), the U.S. Civilian Research and Development Foundation for the Independent States of the Former Soviet Union, the US-Hungarian Fulbright Foundation for Educational Exchange, and the US-Israel Binational Science Foundation.

Appendix A: Details on the calculation of $\langle p_T^2 \rangle$

1. Fitting The J/ψ Invariant Yields

The J/ψ invariant yields as a function of p_T were fitted with a modified Kaplan function of the form

$$f(p_T) = p_0 \left(1 - \left(\frac{p_T}{p_1}\right)^2\right)^{p_2}. \tag{A1}$$

The data points were compared to the integral of the function over the p_T bin when calculating the χ^2. The fit results, along with the ratio of the data to the fit are shown in Fig. 15 for p+p collisions and Figure 16 for 0–100% centrality integrated d+Au collisions. The fit results for each centrality bin are shown in Figs. 17, 18, and 19 for backward, mid, and forward rapidities, respectively.

2. Calculating the Correction Factor k

To account for the fact that the experimental upper p_T limits on the J/ψ invariant yield distributions vary with rapidity and centrality, a correction factor was calculated using the fits described in Sec. A 1. The ratio

$$k = \frac{\langle p_T^2 \rangle [0, \infty]}{\langle p_T^2 \rangle [0, {p_T}^{\max}]} \tag{A2}$$

was calculated from the fit and applied to the numerically calculated $\langle p_T^2 \rangle|_{p_T \le p_T^{\max}}$. The correction factors are shown in Table VI, and are in all cases small ($k < 1.03$). The uncertainty on k is derived from the fit uncertainty by varying the data points within their statistical uncertainties, refitting, and thereby finding the variation in k.

3. Propagating the Type B uncertainties to $\langle p_T^2 \rangle$

When propagating the Type B systematic uncertainties on the J/ψ invariant yields to the calculated $\langle p_T^2 \rangle$ values, the type B uncertainties are assumed to be normally distributed. With this assumption we independently sample the uncertainty distribution of the first and the last data point of the p_T distribution. We then assume the Type B uncertainties are linearly correlated

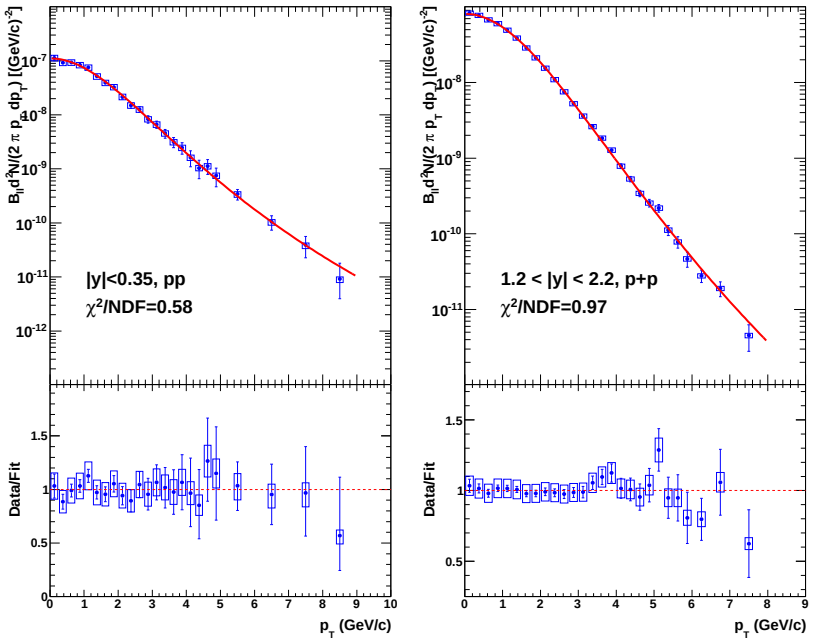

FIG. 15: (Color Online) Results of modified Kaplan fits to midrapidity p+p (Left) and forward rapidity p+p (Right).

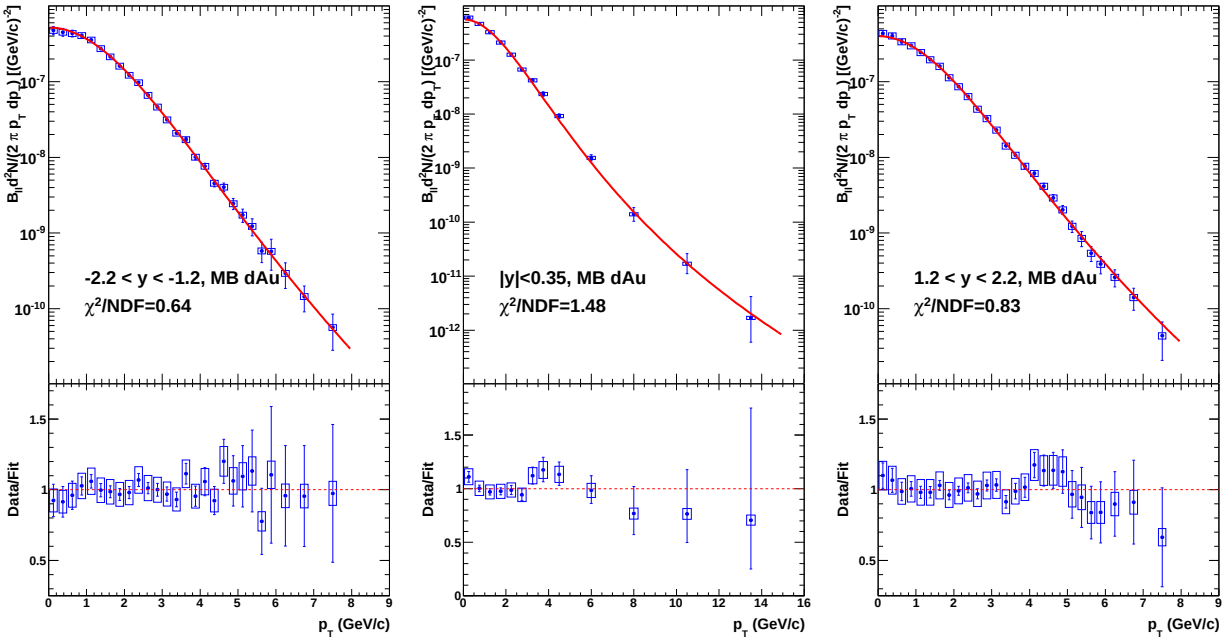

FIG. 16: (Color Online) Results of modified Kaplan fits to backward rapidity 0–100% d+Au (Left), midrapidity 0-100% d+Au (Center), and forward rapidity 0-100% d+Au (Right).

between these two values. The resulting distribution of the $\langle p_T^2 \rangle$ values that arises from this procedure gives an estimate of the effect of the Type B uncertainties on the value of $\langle p_T^2 \rangle$.

The Type C systematic uncertainties on the J/ψ invariant yields do not affect the calculation of $\langle p_T^2 \rangle$. The Type C uncertainties are a global uncertainty, which cancels in the calculation.

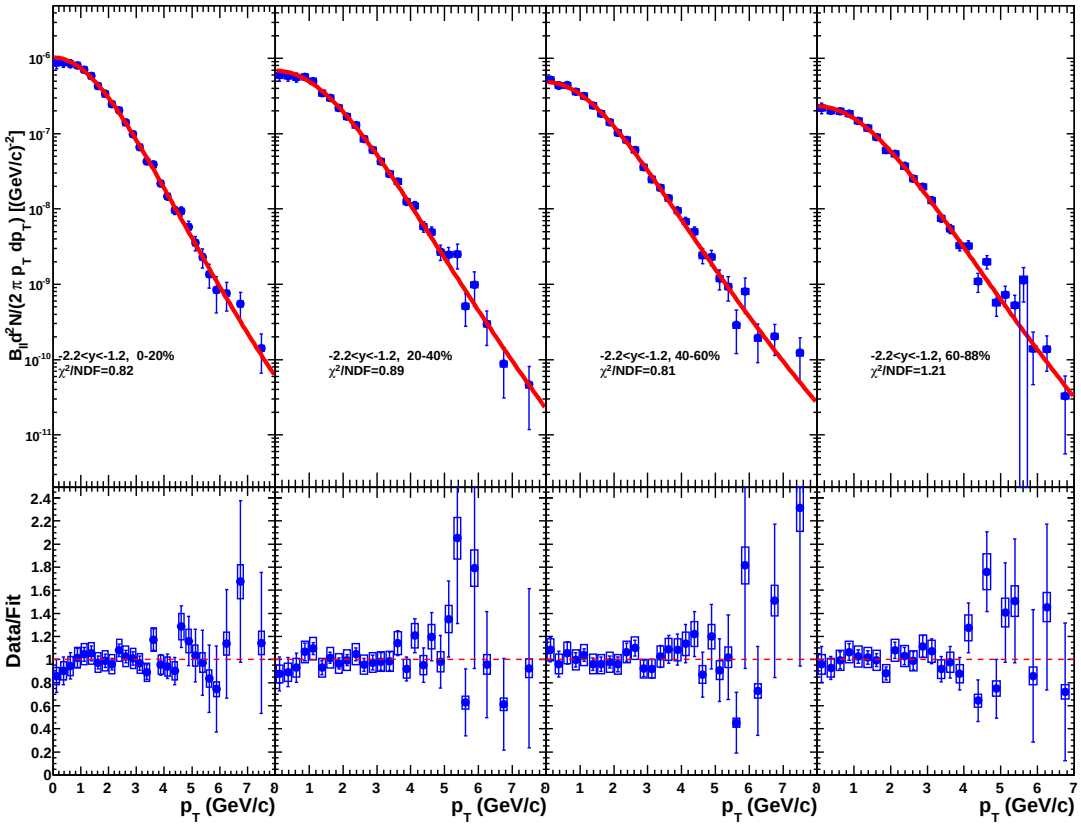

FIG. 17: (Color Online) Results of modified Kaplan fits to backward rapidity d+Au collisions for each centrality.

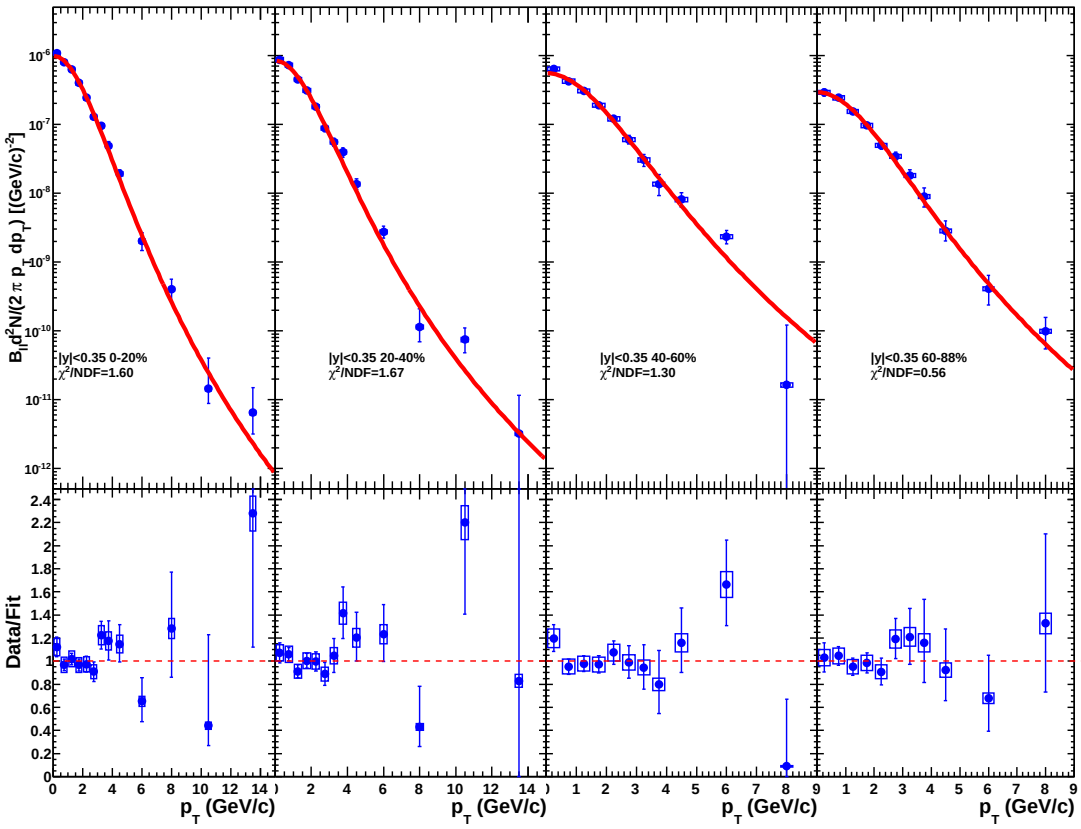

FIG. 18: (Color Online) Results of modified Kaplan fits to midrapidity d+Au collisions for each centrality.

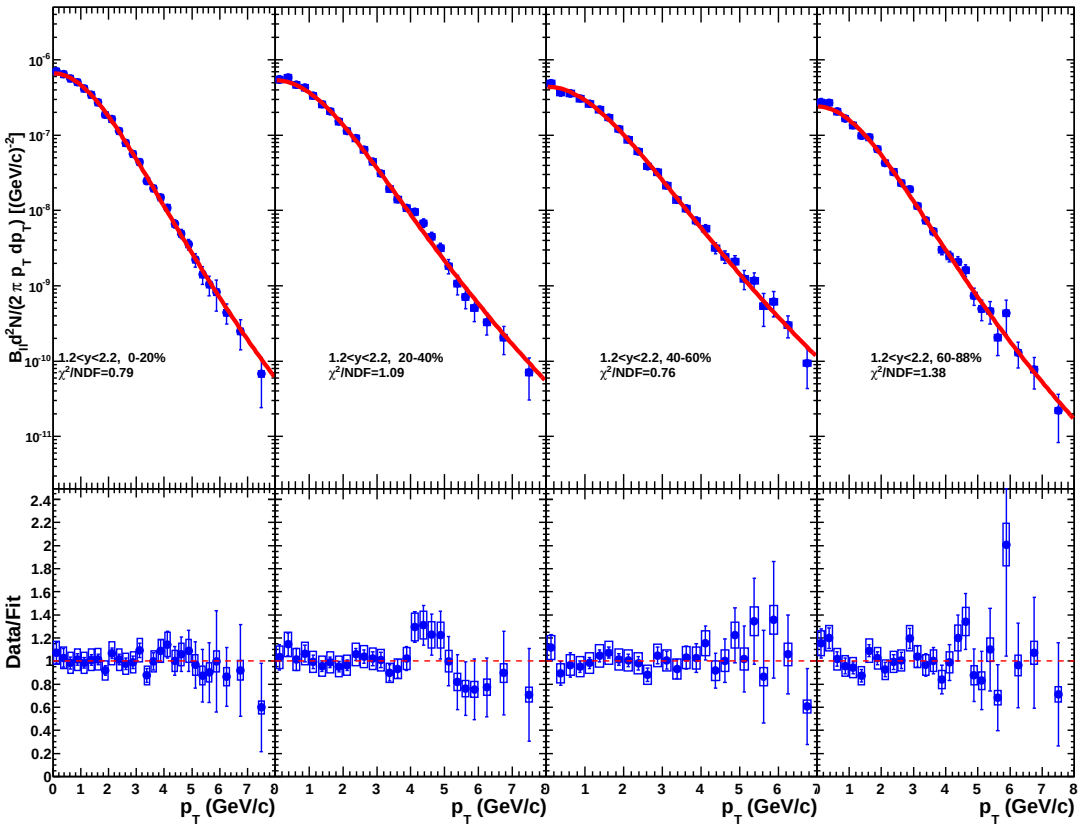

FIG. 19: (Color Online) Results of modified Kaplan fits to forward rapidity d+Au collisions for each centrality.

TABLE VI: $\langle p_T^2 \rangle$ correction factors, k, for p+p and d+Au collisions.

System	y range	Centrality	k
p+p	$1.2 < \|y\| < 2.2$		1.006±0.001
p+p	$\|y\| < 0.35$		1.018±0.007
d+Au	$-2.2 < y < -1.2$	0–100%	1.005±0.001
d+Au	$\|y\| < 0.35$	0–100%	1.002±0.001
d+Au	$1.2 < y < 2.2$	0–100%	1.010±0.002
d+Au	$-2.2 < y < -1.2$	0–20%	1.005±0.002
d+Au	$-2.2 < y < -1.2$	20–40%	1.002±0.001
d+Au	$-2.2 < y < -1.2$	40–60%	1.006±0.002
d+Au	$-2.2 < y < -1.2$	60–88%	1.008±0.003
d+Au	$\|y\| < 0.35$	0–20%	1.001±0.001
d+Au	$\|y\| < 0.35$	20–40%	1.002±0.002
d+Au	$\|y\| < 0.35$	40–60%	1.024±0.017
d+Au	$\|y\| < 0.35$	60–88%	1.020±0.024
d+Au	$1.2 < y < 2.2$	0–20%	1.009±0.003
d+Au	$1.2 < y < 2.2$	20–40%	1.012±0.003
d+Au	$1.2 < y < 2.2$	40–60%	1.023±0.006
d+Au	$1.2 < y < 2.2$	60–88%	1.010±0.004

Appendix B: Data Tables

TABLE VII: Data tables for 0–100% centrality-integrated $R_{d\mathrm{Au}}$ at $-2.2 < y < -1.2$.

p_T [GeV/c]	$R_{d\mathrm{Au}}$	Type A	Type B	Type C
0.00 - 0.25	0.759	±0.1	±0.053	±0.063
0.25 - 0.50	0.772	±0.094	±0.054	±0.064
0.50 - 0.75	0.853	±0.092	±0.059	±0.071
0.75 - 1.00	0.899	±0.06	±0.062	±0.074
1.00 - 1.25	0.955	±0.048	±0.065	±0.079
1.25 - 1.50	0.934	±0.048	±0.064	±0.077
1.50 - 1.75	0.988	±0.048	±0.068	±0.082
1.75 - 2.00	1.000	±0.049	±0.069	±0.083
2.00 - 2.25	1.043	±0.054	±0.072	±0.086
2.25 - 2.50	1.182	±0.061	±0.081	±0.098
2.50 - 2.75	1.159	±0.059	±0.08	±0.096
2.75 - 3.00	1.161	±0.067	±0.08	±0.096
3.00 - 3.25	1.150	±0.075	±0.079	±0.095
3.25 - 3.50	1.059	±0.076	±0.073	±0.088
3.50 - 3.75	1.234	±0.101	±0.085	±0.102
3.75 - 4.00	1.043	±0.098	±0.072	±0.086
4.00 - 4.25	1.285	±0.15	±0.089	±0.106
4.25 - 4.50	1.133	±0.152	±0.078	±0.094
4.50 - 4.75	1.556	±0.252	±0.108	±0.129
4.75 - 5.00	1.265	±0.256	±0.089	±0.105
5.00 - 5.50	1.186	±0.303	±0.083	±0.098
5.50 - 6.00	1.227	±0.518	±0.085	±0.101
6.00 - 7.00	1.228	±0.537	±0.085	±0.102
7.00 - 8.00	1.643	±1.036	±0.116	±0.136

TABLE VIII: Data tables for 0–100% centrality-integrated $R_{d\mathrm{Au}}$ at $|y| < 0.35$.

p_T [GeV/c]	$R_{d\mathrm{Au}}$	Type A	Type B	Type C
0.0 - 0.5	0.78	±0.065	±0.11	±0.061
0.5 - 1.0	0.69	±0.036	±0.094	±0.055
1.0 - 1.5	0.68	±0.035	±0.092	±0.053
1.5 - 2.0	0.78	±0.048	±0.1	±0.061
2.0 - 2.5	0.90	±0.076	±0.12	±0.071
2.5 - 3.0	0.84	±0.092	±0.11	±0.066
3.0 - 3.5	1.00	±0.14	±0.13	±0.078
3.5 - 4.0	1.10	±0.21	±0.15	±0.087
4.0 - 5.0	1.10	$^{+0.22}_{-0.21}$	±0.14	±0.084
5.0 - 7.0	0.91	±0.21	$^{+0.11}_{-0.13}$	±0.072
7.0 - 9.0	0.77	$^{+0.4}_{-0.34}$	$^{+0.09}_{-0.12}$	±0.06

TABLE IX: Data tables for 0–100% centrality-integrated $R_{d\mathrm{Au}}$ at $1.2 < y < 2.2$.

p_T [GeV/c]	$R_{d\mathrm{Au}}$	Type A	Type B	Type C
0.00 - 0.25	0.693	±0.064	±0.052	±0.057
0.25 - 0.50	0.690	±0.059	±0.052	±0.057
0.50 - 0.75	0.664	±0.048	±0.05	±0.055
0.75 - 1.00	0.659	±0.037	±0.049	±0.054
1.00 - 1.25	0.652	±0.032	±0.048	±0.054
1.25 - 1.50	0.671	±0.032	±0.05	±0.055
1.50 - 1.75	0.739	±0.029	±0.055	±0.061
1.75 - 2.00	0.703	±0.029	±0.052	±0.058
2.00 - 2.25	0.732	±0.031	±0.054	±0.061
2.25 - 2.50	0.772	±0.035	±0.057	±0.064
2.50 - 2.75	0.764	±0.037	±0.057	±0.063
2.75 - 3.00	0.821	±0.043	±0.061	±0.068
3.00 - 3.25	0.844	±0.049	±0.063	±0.07
3.25 - 3.50	0.716	±0.048	±0.053	±0.059
3.50 - 3.75	0.765	±0.056	±0.057	±0.063
3.75 - 4.00	0.786	±0.07	±0.059	±0.065
4.00 - 4.25	1.032	±0.107	±0.077	±0.085
4.25 - 4.50	1.030	±0.129	±0.077	±0.085
4.50 - 4.75	1.118	±0.166	±0.084	±0.092
4.75 - 5.00	1.047	±0.186	±0.079	±0.087
5.00 - 5.50	0.836	±0.195	±0.063	±0.069
5.50 - 6.00	0.984	±0.298	±0.074	±0.081
6.00 - 7.00	1.122	±0.387	±0.084	±0.093
7.00 - 8.00	1.275	±0.83	±0.097	±0.105

TABLE X: Data tables for $R_{d\mathrm{Au}}$ as a function of p_T for 0–20% centrality.

y	p_T [GeV/c]	$R_{d\mathrm{Au}}$	Type A	Type B	Type C
$-2.2 < y < -1.2$	0.00 - 0.25	0.702	±0.121	±0.049	±0.063
$-2.2 < y < -1.2$	0.25 - 0.50	0.760	±0.104	±0.053	±0.068
$-2.2 < y < -1.2$	0.50 - 0.75	0.840	±0.105	±0.058	±0.075
$-2.2 < y < -1.2$	0.75 - 1.00	0.894	±0.076	±0.062	±0.08
$-2.2 < y < -1.2$	1.00 - 1.25	0.954	±0.059	±0.065	±0.085
$-2.2 < y < -1.2$	1.25 - 1.50	1.008	±0.066	±0.069	±0.09
$-2.2 < y < -1.2$	1.50 - 1.75	1.000	±0.061	±0.069	±0.089
$-2.2 < y < -1.2$	1.75 - 2.00	1.058	±0.066	±0.073	±0.095
$-2.2 < y < -1.2$	2.00 - 2.25	1.058	±0.062	±0.073	±0.095
$-2.2 < y < -1.2$	2.25 - 2.50	1.252	±0.072	±0.086	±0.112
$-2.2 < y < -1.2$	2.50 - 2.75	1.240	±0.076	±0.085	±0.111
$-2.2 < y < -1.2$	2.75 - 3.00	1.249	±0.083	±0.086	±0.112
$-2.2 < y < -1.2$	3.00 - 3.25	1.230	±0.095	±0.085	±0.11
$-2.2 < y < -1.2$	3.25 - 3.50	1.088	±0.093	±0.075	±0.097
$-2.2 < y < -1.2$	3.50 - 3.75	1.406	±0.13	±0.097	±0.126
$-2.2 < y < -1.2$	3.75 - 4.00	1.131	±0.124	±0.078	±0.101
$-2.2 < y < -1.2$	4.00 - 4.25	1.244	±0.165	±0.086	±0.111
$-2.2 < y < -1.2$	4.25 - 4.50	1.209	±0.186	±0.084	±0.108
$-2.2 < y < -1.2$	4.50 - 4.75	1.824	±0.314	±0.127	±0.163
$-2.2 < y < -1.2$	4.75 - 5.00	1.508	±0.329	±0.106	±0.135
$-2.2 < y < -1.2$	5.00 - 5.50	1.182	±0.33	±0.082	±0.106
$-2.2 < y < -1.2$	5.50 - 6.00	1.171	±0.522	±0.082	±0.105
$-2.2 < y < -1.2$	6.00 - 7.00	1.848	±0.83	±0.128	±0.165
$-2.2 < y < -1.2$	7.00 - 8.00	2.079	±1.364	±0.146	±0.186
$\|y\| < 0.35$	0.0 - 0.5	0.69	±0.071	±0.094	±0.059
$\|y\| < 0.35$	0.5 - 1.0	0.60	±0.04	±0.081	±0.051
$\|y\| < 0.35$	1.0 - 1.5	0.65	±0.042	±0.088	±0.056
$\|y\| < 0.35$	1.5 - 2.0	0.73	±0.054	±0.097	±0.062
$\|y\| < 0.35$	2.0 - 2.5	0.88	±0.088	±0.12	±0.075
$\|y\| < 0.35$	2.5 - 2.0	0.81	±0.11	±0.11	±0.07
$\|y\| < 0.35$	2.0 - 3.5	1.10	±0.17	±0.15	±0.096
$\|y\| < 0.35$	3.5 - 4.0	1.10	$^{+0.25}_{-0.24}$	±0.15	±0.098
$\|y\| < 0.35$	4.0 - 5.0	1.10	$^{+0.26}_{-0.24}$	±0.15	±0.095
$\|y\| < 0.35$	5.0 - 7.0	0.59	$^{+0.21}_{-0.19}$	$^{+0.073}_{-0.087}$	±0.051
$\|y\| < 0.35$	7.0 - 9.0	1.10	$^{+0.61}_{-0.54}$	$^{+0.13}_{-0.17}$	±0.095
$1.2 < y < 2.2$	0.00 - 0.25	0.566	±0.054	±0.042	±0.051
$1.2 < y < 2.2$	0.25 - 0.50	0.557	±0.046	±0.042	±0.05
$1.2 < y < 2.2$	0.50 - 0.75	0.557	±0.034	±0.042	±0.05
$1.2 < y < 2.2$	0.75 - 1.00	0.563	±0.031	±0.042	±0.05
$1.2 < y < 2.2$	1.00 - 1.25	0.559	±0.029	±0.042	±0.05
$1.2 < y < 2.2$	1.25 - 1.50	0.594	±0.029	±0.044	±0.053
$1.2 < y < 2.2$	1.50 - 1.75	0.634	±0.031	±0.047	±0.057
$1.2 < y < 2.2$	1.75 - 2.00	0.587	±0.029	±0.044	±0.052
$1.2 < y < 2.2$	2.00 - 2.25	0.698	±0.034	±0.052	±0.062
$1.2 < y < 2.2$	2.25 - 2.50	0.691	±0.037	±0.051	±0.062
$1.2 < y < 2.2$	2.50 - 2.75	0.691	±0.041	±0.052	±0.062
$1.2 < y < 2.2$	2.75 - 3.00	0.713	±0.047	±0.053	±0.064
$1.2 < y < 2.2$	3.00 - 3.25	0.812	±0.056	±0.061	±0.073
$1.2 < y < 2.2$	3.25 - 3.50	0.631	±0.052	±0.047	±0.056
$1.2 < y < 2.2$	3.50 - 3.75	0.708	±0.064	±0.053	±0.063
$1.2 < y < 2.2$	3.75 - 4.00	0.772	±0.081	±0.058	±0.069
$1.2 < y < 2.2$	4.00 - 4.25	0.922	±0.112	±0.069	±0.083
$1.2 < y < 2.2$	4.25 - 4.50	0.834	±0.124	±0.062	±0.075
$1.2 < y < 2.2$	4.50 - 4.75	0.953	±0.163	±0.071	±0.085
$1.2 < y < 2.2$	4.75 - 5.00	0.922	±0.183	±0.07	±0.082
$1.2 < y < 2.2$	5.00 - 5.50	0.735	±0.192	±0.055	±0.066
$1.2 < y < 2.2$	5.50 - 6.00	0.997	±0.396	±0.075	±0.089
$1.2 < y < 2.2$	6.00 - 7.00	0.971	±0.378	±0.073	±0.087
$1.2 < y < 2.2$	7.00 - 8.00	0.989	±0.739	±0.075	±0.089

TABLE XI: Data tables for $R_{d\mathrm{Au}}$ as a function of p_T for 20–40% centrality.

y	p_T [GeV/c]	$R_{d\mathrm{Au}}$	Type A	Type B	Type C
$-2.2 < y < -1.2$	0.00 - 0.25	0.706	±0.123	±0.049	±0.06
$-2.2 < y < -1.2$	0.25 - 0.50	0.739	±0.108	±0.052	±0.063
$-2.2 < y < -1.2$	0.50 - 0.75	0.815	±0.113	±0.057	±0.07
$-2.2 < y < -1.2$	0.75 - 1.00	0.925	±0.069	±0.064	±0.079
$-2.2 < y < -1.2$	1.00 - 1.25	0.984	±0.051	±0.068	±0.084
$-2.2 < y < -1.2$	1.25 - 1.50	0.874	±0.059	±0.06	±0.075
$-2.2 < y < -1.2$	1.50 - 1.75	1.021	±0.054	±0.07	±0.087
$-2.2 < y < -1.2$	1.75 - 2.00	1.008	±0.054	±0.069	±0.086
$-2.2 < y < -1.2$	2.00 - 2.25	1.067	±0.06	±0.073	±0.091
$-2.2 < y < -1.2$	2.25 - 2.50	1.169	±0.072	±0.08	±0.1
$-2.2 < y < -1.2$	2.50 - 2.75	1.103	±0.073	±0.076	±0.094
$-2.2 < y < -1.2$	2.75 - 3.00	1.137	±0.084	±0.078	±0.097
$-2.2 < y < -1.2$	3.00 - 3.25	1.160	±0.101	±0.08	±0.099
$-2.2 < y < -1.2$	3.25 - 3.50	1.099	±0.102	±0.076	±0.094
$-2.2 < y < -1.2$	3.50 - 3.75	1.234	±0.131	±0.085	±0.106
$-2.2 < y < -1.2$	3.75 - 4.00	0.957	±0.121	±0.066	±0.082
$-2.2 < y < -1.2$	4.00 - 4.25	1.376	±0.195	±0.095	±0.118
$-2.2 < y < -1.2$	4.25 - 4.50	1.077	±0.19	±0.075	±0.092
$-2.2 < y < -1.2$	4.50 - 4.75	1.401	±0.28	±0.097	±0.12
$-2.2 < y < -1.2$	4.75 - 5.00	1.028	±0.266	±0.072	±0.088
$-2.2 < y < -1.2$	5.00 - 5.50	1.481	±0.496	±0.103	±0.127
$-2.2 < y < -1.2$	5.50 - 6.00	1.188	±0.641	±0.083	±0.102
$-2.2 < y < -1.2$	6.00 - 7.00	0.793	±0.469	±0.055	±0.068
$-2.2 < y < -1.2$	7.00 - 8.00	0.996	±0.836	±0.07	±0.085
$\|y\| < 0.35$	0.0 - 0.5	0.83	±0.089	±0.11	±0.068
$\|y\| < 0.35$	0.5 - 1.0	0.80	±0.055	±0.11	±0.065
$\|y\| < 0.35$	1.0 - 1.5	0.69	±0.05	±0.093	±0.056
$\|y\| < 0.35$	1.5 - 2.0	0.85	±0.069	±0.11	±0.069
$\|y\| < 0.35$	2.0 - 2.5	0.97	±0.11	±0.13	±0.079
$\|y\| < 0.35$	2.5 - 2.0	0.82	±0.12	±0.11	±0.067
$\|y\| < 0.35$	2.0 - 3.5	0.97	±0.18	±0.13	±0.079
$\|y\| < 0.35$	3.5 - 4.0	1.40	±0.31	±0.18	±0.11
$\|y\| < 0.35$	4.0 - 5.0	1.20	$^{+0.3}_{-0.28}$	±0.16	±0.096
$\|y\| < 0.35$	5.0 - 7.0	1.20	$^{+0.33}_{-0.32}$	$^{+0.15}_{-0.18}$	±0.098
$\|y\| < 0.35$	7.0 - 9.0	0.47	$^{+0.43}_{-0.25}$	$^{+0.054}_{-0.071}$	±0.038
$1.2 < y < 2.2$	0.00 - 0.25	0.649	±0.076	±0.049	±0.056
$1.2 < y < 2.2$	0.25 - 0.50	0.735	±0.066	±0.056	±0.063
$1.2 < y < 2.2$	0.50 - 0.75	0.680	±0.065	±0.051	±0.058
$1.2 < y < 2.2$	0.75 - 1.00	0.697	±0.05	±0.052	±0.06
$1.2 < y < 2.2$	1.00 - 1.25	0.661	±0.042	±0.049	±0.057
$1.2 < y < 2.2$	1.25 - 1.50	0.653	±0.035	±0.048	±0.056
$1.2 < y < 2.2$	1.50 - 1.75	0.712	±0.037	±0.053	±0.061
$1.2 < y < 2.2$	1.75 - 2.00	0.701	±0.037	±0.052	±0.06
$1.2 < y < 2.2$	2.00 - 2.25	0.716	±0.039	±0.053	±0.061
$1.2 < y < 2.2$	2.25 - 2.50	0.818	±0.047	±0.061	±0.07
$1.2 < y < 2.2$	2.50 - 2.75	0.831	±0.052	±0.062	±0.071
$1.2 < y < 2.2$	2.75 - 3.00	0.831	±0.057	±0.062	±0.071
$1.2 < y < 2.2$	3.00 - 3.25	0.844	±0.065	±0.063	±0.072
$1.2 < y < 2.2$	3.25 - 3.50	0.728	±0.066	±0.054	±0.062
$1.2 < y < 2.2$	3.50 - 3.75	0.752	±0.075	±0.056	±0.064
$1.2 < y < 2.2$	3.75 - 4.00	0.819	±0.095	±0.061	±0.07
$1.2 < y < 2.2$	4.00 - 4.25	1.191	±0.148	±0.089	±0.102
$1.2 < y < 2.2$	4.25 - 4.50	1.252	±0.192	±0.094	±0.107
$1.2 < y < 2.2$	4.50 - 4.75	1.276	±0.223	±0.096	±0.109
$1.2 < y < 2.2$	4.75 - 5.00	1.206	±0.247	±0.091	±0.103
$1.2 < y < 2.2$	5.00 - 5.50	0.859	±0.237	±0.065	±0.074
$1.2 < y < 2.2$	5.50 - 6.00	0.960	±0.356	±0.072	±0.082
$1.2 < y < 2.2$	6.00 - 7.00	1.111	±0.448	±0.083	±0.095
$1.2 < y < 2.2$	7.00 - 8.00	1.519	±1.038	±0.115	±0.13

TABLE XII: Data tables for $R_{d\mathrm{Au}}$ as a function of p_T for 40–60% centrality.

y	p_T [GeV/c]	$R_{d\mathrm{Au}}$	Type A	Type B	Type C
$-2.2 < y < -1.2$	0.00 - 0.25	0.953	±0.103	±0.066	±0.087
$-2.2 < y < -1.2$	0.25 - 0.50	0.865	±0.104	±0.061	±0.079
$-2.2 < y < -1.2$	0.50 - 0.75	0.995	±0.094	±0.069	±0.09
$-2.2 < y < -1.2$	0.75 - 1.00	0.920	±0.06	±0.063	±0.084
$-2.2 < y < -1.2$	1.00 - 1.25	0.976	±0.055	±0.067	±0.089
$-2.2 < y < -1.2$	1.25 - 1.50	0.929	±0.056	±0.064	±0.084
$-2.2 < y < -1.2$	1.50 - 1.75	0.979	±0.067	±0.067	±0.089
$-2.2 < y < -1.2$	1.75 - 2.00	1.018	±0.06	±0.07	±0.093
$-2.2 < y < -1.2$	2.00 - 2.25	1.015	±0.074	±0.07	±0.092
$-2.2 < y < -1.2$	2.25 - 2.50	1.159	±0.091	±0.08	±0.105
$-2.2 < y < -1.2$	2.50 - 2.75	1.227	±0.086	±0.085	±0.112
$-2.2 < y < -1.2$	2.75 - 3.00	1.036	±0.088	±0.071	±0.094
$-2.2 < y < -1.2$	3.00 - 3.25	1.046	±0.101	±0.072	±0.095
$-2.2 < y < -1.2$	3.25 - 3.50	1.114	±0.114	±0.077	±0.101
$-2.2 < y < -1.2$	3.50 - 3.75	1.152	±0.14	±0.08	±0.105
$-2.2 < y < -1.2$	3.75 - 4.00	1.124	±0.153	±0.078	±0.102
$-2.2 < y < -1.2$	4.00 - 4.25	1.313	±0.212	±0.091	±0.119
$-2.2 < y < -1.2$	4.25 - 4.50	1.427	±0.253	±0.099	±0.13
$-2.2 < y < -1.2$	4.50 - 4.75	1.080	±0.263	±0.075	±0.098
$-2.2 < y < -1.2$	4.75 - 5.00	1.365	±0.356	±0.096	±0.124
$-2.2 < y < -1.2$	5.00 - 5.50	0.985	±0.345	±0.069	±0.09
$-2.2 < y < -1.2$	5.50 - 6.00	1.354	±0.796	±0.094	±0.123
$-2.2 < y < -1.2$	6.00 - 7.00	1.297	±0.671	±0.09	±0.118
$-2.2 < y < -1.2$	7.00 - 8.00	4.130	±2.905	±0.291	±0.375
$\lvert y\rvert < 0.35$	0.0 - 0.5	0.94	±0.11	±0.13	±0.082
$\lvert y\rvert < 0.35$	0.5 - 1.0	0.73	±0.059	±0.098	±0.063
$\lvert y\rvert < 0.35$	1.0 - 1.5	0.73	±0.059	±0.099	±0.064
$\lvert y\rvert < 0.35$	1.5 - 2.0	0.80	±0.074	±0.11	±0.07
$\lvert y\rvert < 0.35$	2.0 - 2.5	0.99	±0.12	±0.14	±0.087
$\lvert y\rvert < 0.35$	2.5 - 2.0	0.87	±0.15	±0.12	±0.076
$\lvert y\rvert < 0.35$	2.0 - 3.5	0.82	$^{+0.2}_{-0.19}$	±0.11	±0.072
$\lvert y\rvert < 0.35$	3.5 - 4.0	0.73	$^{+0.29}_{-0.26}$	±0.098	±0.064
$\lvert y\rvert < 0.35$	4.0 - 5.0	1.10	$^{+0.34}_{-0.3}$	±0.14	±0.094
$\lvert y\rvert < 0.35$	5.0 - 7.0	1.60	$^{+0.47}_{-0.45}$	$^{+0.2}_{-0.23}$	±0.14
$\lvert y\rvert < 0.35$	7.0 - 9.0	0.10	$^{+0.67}_{-0.51}$	±0.012	±0.009
$1.2 < y < 2.2$	0.00 - 0.25	0.897	±0.098	±0.067	±0.082
$1.2 < y < 2.2$	0.25 - 0.50	0.731	±0.087	±0.055	±0.067
$1.2 < y < 2.2$	0.50 - 0.75	0.816	±0.093	±0.061	±0.074
$1.2 < y < 2.2$	0.75 - 1.00	0.778	±0.046	±0.058	±0.071
$1.2 < y < 2.2$	1.00 - 1.25	0.802	±0.042	±0.06	±0.073
$1.2 < y < 2.2$	1.25 - 1.50	0.862	±0.046	±0.064	±0.078
$1.2 < y < 2.2$	1.50 - 1.75	0.916	±0.045	±0.068	±0.083
$1.2 < y < 2.2$	1.75 - 2.00	0.865	±0.047	±0.064	±0.079
$1.2 < y < 2.2$	2.00 - 2.25	0.859	±0.051	±0.064	±0.078
$1.2 < y < 2.2$	2.25 - 2.50	0.854	±0.056	±0.064	±0.078
$1.2 < y < 2.2$	2.50 - 2.75	0.781	±0.057	±0.058	±0.071
$1.2 < y < 2.2$	2.75 - 3.00	0.933	±0.072	±0.069	±0.085
$1.2 < y < 2.2$	3.00 - 3.25	0.907	±0.079	±0.068	±0.082
$1.2 < y < 2.2$	3.25 - 3.50	0.807	±0.081	±0.06	±0.073
$1.2 < y < 2.2$	3.50 - 3.75	0.878	±0.096	±0.066	±0.08
$1.2 < y < 2.2$	3.75 - 4.00	0.868	±0.115	±0.065	±0.079
$1.2 < y < 2.2$	4.00 - 4.25	1.109	±0.161	±0.083	±0.101
$1.2 < y < 2.2$	4.25 - 4.50	0.911	±0.167	±0.068	±0.083
$1.2 < y < 2.2$	4.50 - 4.75	1.082	±0.23	±0.081	±0.098
$1.2 < y < 2.2$	4.75 - 5.00	1.246	±0.281	±0.094	±0.113
$1.2 < y < 2.2$	5.00 - 5.50	1.114	±0.343	±0.084	±0.101
$1.2 < y < 2.2$	5.50 - 6.00	1.417	±0.632	±0.107	±0.129
$1.2 < y < 2.2$	6.00 - 7.00	1.268	±0.55	±0.095	±0.115
$1.2 < y < 2.2$	7.00 - 8.00	0.747	±7.473e+39	±0.057	±0.068

TABLE XIII: Data tables for $R_{d\mathrm{Au}}$ as a function of p_T for 60–88% centrality.

y	p_T [GeV/c]	$R_{d\mathrm{Au}}$	Type A	Type B	Type C
$-2.2 < y < -1.2$	0.00 - 0.25	0.829	±0.14	±0.057	±0.088
$-2.2 < y < -1.2$	0.25 - 0.50	0.823	±0.091	±0.058	±0.088
$-2.2 < y < -1.2$	0.50 - 0.75	0.922	±0.074	±0.064	±0.098
$-2.2 < y < -1.2$	0.75 - 1.00	0.965	±0.068	±0.066	±0.103
$-2.2 < y < -1.2$	1.00 - 1.25	0.947	±0.057	±0.065	±0.101
$-2.2 < y < -1.2$	1.25 - 1.50	0.965	±0.059	±0.066	±0.103
$-2.2 < y < -1.2$	1.50 - 1.75	0.990	±0.058	±0.068	±0.105
$-2.2 < y < -1.2$	1.75 - 2.00	0.888	±0.059	±0.061	±0.095
$-2.2 < y < -1.2$	2.00 - 2.25	1.097	±0.077	±0.075	±0.117
$-2.2 < y < -1.2$	2.25 - 2.50	1.073	±0.084	±0.074	±0.114
$-2.2 < y < -1.2$	2.50 - 2.75	1.047	±0.09	±0.072	±0.111
$-2.2 < y < -1.2$	2.75 - 3.00	1.175	±0.107	±0.081	±0.125
$-2.2 < y < -1.2$	3.00 - 3.25	1.132	±0.122	±0.078	±0.12
$-2.2 < y < -1.2$	3.25 - 3.50	0.908	±0.115	±0.063	±0.097
$-2.2 < y < -1.2$	3.50 - 3.75	0.926	±0.138	±0.064	±0.099
$-2.2 < y < -1.2$	3.75 - 4.00	0.804	±0.136	±0.056	±0.086
$-2.2 < y < -1.2$	4.00 - 4.25	1.277	±0.234	±0.088	±0.136
$-2.2 < y < -1.2$	4.25 - 4.50	0.642	±0.187	±0.044	±0.068
$-2.2 < y < -1.2$	4.50 - 4.75	1.827	±0.401	±0.127	±0.194
$-2.2 < y < -1.2$	4.75 - 5.00	0.700	±0.251	±0.049	±0.075
$-2.2 < y < -1.2$	5.00 - 5.50	1.193	±0.42	±0.083	±0.127
$-2.2 < y < -1.2$	5.50 - 6.00	3.141	±1.737	±0.219	±0.334
$-2.2 < y < -1.2$	6.00 - 7.00	1.122	±0.714	±0.078	±0.119
$-2.2 < y < -1.2$	7.00 - 8.00	0.443	±4.427e+39	±0.031	±0.047
$\lvert y\rvert < 0.35$	0.0 - 0.5	0.91	±0.13	±0.12	±0.094
$\lvert y\rvert < 0.35$	0.5 - 1.0	0.88	±0.077	±0.12	±0.091
$\lvert y\rvert < 0.35$	1.0 - 1.5	0.77	±0.069	±0.1	±0.08
$\lvert y\rvert < 0.35$	1.5 - 2.0	0.86	±0.089	±0.11	±0.089
$\lvert y\rvert < 0.35$	2.0 - 2.5	0.87	±0.13	±0.12	±0.09
$\lvert y\rvert < 0.35$	2.5 - 2.0	1.10	±0.18	±0.14	±0.11
$\lvert y\rvert < 0.35$	2.0 - 3.5	1.00	±0.24	±0.14	±0.11
$\lvert y\rvert < 0.35$	3.5 - 4.0	1.00	$^{+0.37}_{-0.35}$	±0.14	±0.11
$\lvert y\rvert < 0.35$	4.0 - 5.0	0.81	$^{+0.34}_{-0.27}$	±0.11	±0.084
$\lvert y\rvert < 0.35$	5.0 - 7.0	0.59	$^{+0.34}_{-0.27}$	$^{+0.073}_{-0.086}$	±0.061
$\lvert y\rvert < 0.35$	7.0 - 9.0	1.30	$^{+0.94}_{-0.75}$	$^{+0.15}_{-0.2}$	±0.14
$1.2 < y < 2.2$	0.00 - 0.25	1.038	±0.123	±0.078	±0.111
$1.2 < y < 2.2$	0.25 - 0.50	1.100	±0.089	±0.083	±0.117
$1.2 < y < 2.2$	0.50 - 0.75	0.961	±0.064	±0.072	±0.102
$1.2 < y < 2.2$	0.75 - 1.00	0.873	±0.065	±0.065	±0.093
$1.2 < y < 2.2$	1.00 - 1.25	0.859	±0.05	±0.064	±0.091
$1.2 < y < 2.2$	1.25 - 1.50	0.800	±0.051	±0.059	±0.085
$1.2 < y < 2.2$	1.50 - 1.75	1.028	±0.054	±0.076	±0.109
$1.2 < y < 2.2$	1.75 - 2.00	0.963	±0.058	±0.072	±0.103
$1.2 < y < 2.2$	2.00 - 2.25	0.864	±0.062	±0.064	±0.092
$1.2 < y < 2.2$	2.25 - 2.50	0.939	±0.068	±0.07	±0.1
$1.2 < y < 2.2$	2.50 - 2.75	0.966	±0.076	±0.072	±0.103
$1.2 < y < 2.2$	2.75 - 3.00	1.146	±0.094	±0.085	±0.122
$1.2 < y < 2.2$	3.00 - 3.25	0.999	±0.097	±0.075	±0.106
$1.2 < y < 2.2$	3.25 - 3.50	0.886	±0.097	±0.066	±0.094
$1.2 < y < 2.2$	3.50 - 3.75	0.897	±0.112	±0.067	±0.096
$1.2 < y < 2.2$	3.75 - 4.00	0.741	±0.116	±0.055	±0.079
$1.2 < y < 2.2$	4.00 - 4.25	0.985	±0.169	±0.074	±0.105
$1.2 < y < 2.2$	4.25 - 4.50	1.228	±0.227	±0.092	±0.131
$1.2 < y < 2.2$	4.50 - 4.75	1.477	±0.305	±0.111	±0.157
$1.2 < y < 2.2$	4.75 - 5.00	0.906	±0.257	±0.068	±0.096
$1.2 < y < 2.2$	5.00 - 5.50	0.913	±0.309	±0.069	±0.097
$1.2 < y < 2.2$	5.50 - 6.00	1.622	±0.816	±0.122	±0.173
$1.2 < y < 2.2$	6.00 - 7.00	1.381	±0.628	±0.103	±0.147
$1.2 < y < 2.2$	7.00 - 8.00	1.527	±1.12	±0.116	±0.163

[1] N. Brambilla, S. Eidelman, B. Heltsley, R. Vogt, G. Bodwin, et al., Eur. Phys. J. C **71**, 1534 (2011).
[2] M. Abreu et al. (NA38 Collaboration), Phys. Lett. B **444**, 516 (1998).
[3] B. Alessandro et al. (NA50 Collaboration), Phys. Lett. B **553**, 167 (2003).
[4] B. Alessandro et al. (NA50 Collaboration), Eur. Phys. J. C **33**, 31 (2004).
[5] B. Alessandro et al. (NA50 Collaboration), Eur. Phys. J. C **48**, 329 (2006).
[6] R. Arnaldi et al. (NA60 Collaboration), Phys. Lett. B **706**, 263 (2012).
[7] M. J. Leitch et al. (FNAL E866/NuSea Collaboration), Phys. Rev. Lett. **84**, 3256 (2000).
[8] I. Abt et al. (HERA-B Collaboration), Eur. Phys. J. C **60**, 525 (2009).
[9] C. Lourenco, R. Vogt, and H. K. Woehri, JHEP **02**, 014 (2009), and references therein.
[10] T. Matsui and H. Satz, Phys. Lett. B **178**, 416 (1986).
[11] R. Arnaldi et al. (NA60 Collaboration), Phys. Rev. Lett. **99**, 132302 (2007).
[12] A. Adare et al. (PHENIX Collaboration), Phys. Rev. Lett. **98**, 232301 (2007).
[13] S. Chatrchyan et al., (CMS Collaboration), arXiv:1201.5069 (2012).
[14] B. Abelev et al., (ALICE Collaboration), arXiv:1202.1383 (2012).
[15] A. Adare et al., (PHENIX Collaboration), arXiv:1105.1966 (2011).
[16] A. Adare et al. (PHENIX Collaboration), Phys. Rev. C **77**, 024912 (2008).
[17] S. S. Adler et al. (PHENIX Collaboration), Phys. Rev. Lett. **96**, 012304 (2006).
[18] A. Adare et al. (PHENIX Collaboration), Phys. Rev. Lett. **107**, 142301 (2011).
[19] K. Adcox et al. (PHENIX Collaboration), Nucl. Instrum. Methods A **499**, 469 (2003).
[20] S. N. White, AIP Conf. Proc. **792**, 527 (2005).
[21] M. L. Miller, K. Reygers, S. J. Sanders, and P. Steinberg, Ann. Rev. Nucl. Part. Sci. **57**, 205 (2007).
[22] A. Spiridonov, hep-ex/0510076 (2005).
[23] T. Sjostrand, S. Mrenna, and P. Z. Skands, JHEP **05**, 026 (2006).
[24] GEANT 3.2.1 Manual (CERN, Geneva, 1993); available at http://wwwasdoc.web.cern.ch/wwwasdoc/pdfdir/geant.pdf.5.
[25] A. Adare et al. (PHENIX Collaboration), Phys. Rev. Lett. **101**, 122301 (2008).
[26] B. Abelev et al. (STAR Collaboration), Phys. Rev. c **80**, 041902 (2009).
[27] E. Ferreiro, F. Fleuret, J. Lansberg, N. Matagne, and A. Rakotozafindrabe, arXiv:1201.5574 (2012).
[28] D. de Florian and R. Sassot, Phys. Rev. D **69**, 074028 (2004).
[29] K. Eskola, V. Kolhinen, and C. Salgado, Eur. Phys. J. C **9**, 61 (1999).
[30] K. J. Eskola, H. Paukkunen, and C. A. Salgado, JHEP **04**, 065 (2009).
[31] J. Cronin, H. J. Frisch, M. Shochet, J. Boymond, R. Mermod, et al., Phys. Rev. D **11**, 3105 (1975).
[32] B. Kopeliovich, I. Potashnikova, and I. Schmidt, Nucl. Phys. A **864**, 203 (2011).
[33] B. Z. Kopeliovich, I. K. Potashnikova, and I. Schmidt, Phys. Rev. C **82**, 024901 (2010).
[34] K. J. Golec-Biernat and M. Wusthoff, Phys. Rev. D **60**, 114023 (1999).
[35] J. L. Nagle, A. D. Frawley, L. A. Linden Levy, and M. G. Wysocki, arXiv:1011.4534 (2011).
[36] E. Ferreiro, F. Fleuret, J. Lansberg, and A. Rakotozafindrabe, Phys. Lett. B **680**, 50 (2009).
[37] K. J. Eskola, H. Paukkunen, and C. A. Salgado, JHEP **0807**, 102 (2008).
[38] J. Aubert et al. (European Muon Collaboration), Phys. Lett. B **123**, 275 (1983).
[39] E. Ferreiro, F. Fleuret, J. Lansberg, N. Matagne, and A. Rakotozafindrabe, arXiv:1110.5047 (2011).
[40] R. Sharma and I. Vitev, arXiv:1203.0329 (2012).
[41] I. Vitev, T. Goldman, M. B. Johnson, and J. W. Qiu, Phys. Rev. D **74**, 054010 (2006).